Present climate characterization and future changes in Clear-Air Turbulence (CAT) over the northern hemisphere

Mohamed Foudad, Emilia Sanchez-Gomez, Mélanie C. Rochoux, Thomas Jaravel, Laurent Terray

Past and Future Trends in Clear-Air Turbulence over the Northern Hemisphere

Mohamed Foudad[1], Emilia Sanchez-Gomez[1], Thomas Jaravel[1], Mélanie C. Rochoux[1], and Laurent Terray[1]

[1]CERFACS

November 8, 2023

Abstract

Clear-Air Turbulence (CAT) is associated with wind shear in the vicinity of jet streams in upper atmospheric levels. This turbulence occurs in cloudless regions and causes most weather-related aircraft accidents. Recent studies have shown that in response to climate change, CAT could significantly increase over certain regions as a consequence of strengthening of jet streams. In this study we use several atmospheric reanalyses and coupled model experiments database to evaluate CAT recent and future changes in the Northern Hemisphere. Several CAT diagnostics are computed to assess the sensitivity of results to different turbulence representations. A significant positive trend in CAT frequency is found in the reanalyses in different regions in the Northern Hemisphere over the period 1980-2021. The signal-to-noise analysis shows that over North Africa, East Asia and Middle East the increase of CAT occurrence in the last decades is likely attributed to global warming. In contrast, over the North Atlantic and North Pacific the internal climate variability is too strong to detect a response to anthropogenic forcing in the observed trends. Future climate projections show that over several regions in the Northern Hemisphere, CAT is projected to increase with a high model agreement and independently of the CAT diagnostic used. The largest increase in CAT is projected to occur over East Asia. In the North Atlantic, large uncertainty remains due to lack of model agreement and differences among the various CAT diagnostics.

Past and Future Trends in Clear-Air Turbulence over the Northern Hemisphere

Mohamed Foudad[1], Emilia Sanchez-Gomez[1], Thomas Jaravel[1], Mélanie C. Rochoux[1], and Laurent Terray[1]

[1]CECI, Université de Toulouse, CERFACS/CNRS, Toulouse, France

Key Points:

- Atmospheric reanalyses show increases in the frequency of Clear-Air Turbulence (CAT) in recent decades over several regions
- The increases over some regions could be attributed to global warming. In the North Atlantic, the increases are due to natural variability
- CAT frequency is projected to increase in the future over East Asia, Middle East, North Africa, North Pacific and North America

Corresponding author: M. Foudad, foudad@cerfacs.fr

Abstract

Clear-Air Turbulence (CAT) is associated with wind shear in the vicinity of jet streams in upper atmospheric levels. This turbulence occurs in cloudless regions and causes most weather-related aircraft accidents. Recent studies have shown that in response to climate change, CAT could significantly increase over certain regions as a consequence of strengthening of jet streams. In this study we use several atmospheric reanalyses and coupled model experiments database to evaluate CAT recent and future changes in the Northern Hemisphere. Several CAT diagnostics are computed to assess the sensitivity of results to different turbulence representations. A significant positive trend in CAT frequency is found in the reanalyses in different regions in the Northern Hemisphere over the period 1980-2021. The signal-to-noise analysis shows that over North Africa, East Asia and Middle East the increase of CAT occurrence in the last decades is likely attributed to global warming. In contrast, over the North Atlantic and North Pacific the internal climate variability is too strong to detect a response to anthropogenic forcing in the observed trends. Future climate projections show that over several regions in the Northern Hemisphere, CAT is projected to increase with a high model agreement and independently of the CAT diagnostic used. The largest increase in CAT is projected to occur over East Asia. In the North Atlantic, large uncertainty remains due to lack of model agreement and differences among the various CAT diagnostics.

Plain Language Summary

Aircrafts in flight can be subject to Clear-Air Turbulence (CAT), which is defined as all turbulence that occurs in the atmosphere away from a visible convective activity, and which is particularly difficult to detect by pilots and using on-board radar. CAT can injure passengers and flight attendants, cause structural damage to planes and induce considerable economic loss. In this study we use several atmospheric reanalyses and coupled model experiments database to evaluate CAT recent and future changes in the Northern Hemisphere. We also compute several CAT diagnostics to evaluate the sensitivity of results to different turbulence representations. Our results show that over several regions in the Northern Hemisphere, in particular East Asia, positive CAT trends are found as a consequence of anthropogenic forcing, indicating that the response of CAT to global warming can be already detectable in the recent decades. Positive trends in CAT frequency are projected to increase for different global warming levels over these regions at aircraft cruising altitudes. Nevertheless, over the North Atlantic region there are still many uncertainties in the response of climate models and also in CAT diagnostics used. The changes in CAT described in this study could have important consequences for aviation safety.

1 Introduction

Atmospheric turbulence is responsible for 71% of all weather-related aircraft accidents (Gultepe et al., 2019). Turbulence events can injure passengers and flight attendants, and in some rare cases, fatalities have occurred (Ellrod et al., 2015). It is also the cause of many people's fear of air travel (Sharman et al., 2012). The number of turbulence-related injuries is probably underestimated, because as pointed by Sharman et al. (2006), not all injuries are reported. Besides, repeated turbulence encounters over the lifetime of the aircraft may lead to material fatigue and can cause structural damage to aircraft (Ellrod et al., 2015). Thus, turbulence encounters are a safety issue, but they also cost to the airlines millions of dollars, and may cause flight delays and increasing fuel consumption and emissions (Sharman & Lane, 2016; P. D. Williams, 2016).

The main sources of atmospheric turbulence are: convective turbulence, mountain wave turbulence, and clear-air turbulence (CAT). In some cases, more specifically over high mountain chains (e.g., Himalayas, Rocky Mountains, Alps), distinguishing CAT from

mountain wave turbulence is unclear. Turbulence in clouds and thunderstorms can easily be detected visually by pilots and using on-board radar. In contrast, CAT is invisible and cannot be seen by pilots or radars, and is particularly difficult to detect and avoid. Because of this, CAT is the major cause of aviation turbulence and has a significant impact on aviation safety (Sharman & Lane, 2016).

CAT is defined as all turbulence that occurs in the atmosphere at altitudes of 5.6 km (∼500 hPa) or higher away from a visible convective activity. This includes turbulence found in cirrus clouds not in or adjacent to visible convective activity (Ellrod et al., 2015; Sharman & Lane, 2016). CAT often occurs near the tropopause level, where jet streams blow from west to east in the midlatitudes of both hemispheres (Dutton & Panofsky, 1970; Ellrod et al., 2015). The principal mechanism of CAT generation is the Kelvin-Helmholtz instability (Dutton & Panofsky, 1970; Ellrod & Knapp, 1992; Sharman & Lane, 2016). Kelvin-Helmholtz instability occurs when vertical wind shear is too strong to overcome the dampening influence of static stability. Vertical wind shear is, therefore, the most important ingredient for generating CAT. The environmental conditions favourable for a large vertical wind shear are found near jet streams and upper-level atmospheric fronts. About two-thirds of CAT occurrences are found near the jet streams (Ellrod et al., 2015). Breaking gravity waves induced by high mountains and by convection contribute also to CAT production (Ellrod et al., 2015; Storer et al., 2019).

Given its negative consequences for aviation safety, operational weather prediction centres provide daily CAT forecasts for airlines and air-navigation service providers. The spatial resolution of current numerical weather prediction models is too coarse to resolve explicitly turbulence (Ellrod & Knapp, 1992; Jaeger & Sprenger, 2007; Sharman & Lane, 2016; Sharman et al., 2006). However, turbulence in the atmosphere that affects aircraft is created by large-scale forcing mechanisms, which can be explicitly resolved by the numerical weather prediction models under the assumption that energy cascades down from larger scales into smaller eddies (Dutton & Panofsky, 1970; Sharman et al., 2006). Therefore, many CAT indices have been developed to diagnose regions where turbulence-generating mechanisms may likely occur, such as regions in which strong vertical and horizontal wind shear, horizontal deformation, and frontogenesis are present.

CAT variations in frequency and intensity are tightly related to jet stream changes at different timescales. In the context of global warming, previous studies have suggested that in response to greenhouse gas (GHGs) forcing, the midlatitude meridional temperature gradient in the upper troposphere may strengthen because of the polar lower-stratospheric cooling and tropical upper-tropospheric warming (J. H. Lee et al., 2023; S. H. Lee et al., 2019; Shaw et al., 2016). In consequence, jet streams and hence vertical wind shears could also increase, potentially inducing changes in CAT (P. D. Williams & Joshi, 2013). Indeed, recent studies have shown that vertical wind shear has increased during the last decades in response to the enhanced upper-level meridional temperature gradient (J. H. Lee et al., 2023; S. H. Lee et al., 2019; Lv et al., 2021). Jaeger and Sprenger (2007) found an increase of 40–90% in CAT frequency over different regions of the Northern Hemisphere by using ERA40 reanalysis (Uppala et al., 2005) in the period 1958-2001. More recently J. H. Lee et al. (2023) used CAT indices applied to ERA5 reanalysis and reported that the most significant increasing trend in CAT frequency during the last decades is located over East Asia. By comparing pre-industrial and doubled-CO2 climate simulations, P. D. Williams (2017) shows that CAT frequency may increase significantly in the future over the North Atlantic region. Storer et al. (2017) used climate future projections from CMIP5 (Coupled Model Intercomparison Project Phase 5) to assess CAT changes at global scale. They show an increase in CAT frequency across the globe, especially in the midlatitudes.

All these studies applied CAT indices to fields issued from atmospheric reanalyses and climate model experiments. Nevertheless, only one reanalysis or a single coupled model is used to evaluate recent and future CAT changes, which represents a limitation to assess

the climate uncertainty. Indeed, the main sources of uncertainties in climate change arise from i) the intrinsic climate variability, also called the internal climate variability; ii) the climate model formulation; and iii) the scenario of emissions (Hawkins & Sutton, 2011). In this study, we take into account the first two climate-related uncertainties while evaluating the past and future changes in CAT over the Northern Hemisphere. In addition, diagnostics used to characterize CAT may be also a source of uncertainty. We use here several atmospheric reanalyses and coupled model experiments from CMIP6, and a large ensemble member of 20 simulations performed with CNRM-CM6-1 model, in order to study the roles of the internal climate variability and the model uncertainty in CAT trends. We also compute several CAT diagnostics to analyse the sensitivity of our results to different turbulence representations. Note that we focus on Moderate-Or-Greater (MOG) CAT, which is known to have the greatest implications for in-flight safety (P. D. Williams & Joshi, 2013; Sharman et al., 2006). The datasets, numerical experiments and methodology are described in Sections 2 and 3, respectively. Results regarding the past and future CAT trends are presented and discussed in Section 4. Finally, in Section 5, the conclusions and prospects for future work are provided.

2 Data

To compute CAT indices, we use daily averages of wind, geopotential height and temperature fields from atmospheric reanalysis and climate model experiments. Three state-of-the-art atmospheric reanalyses in the period 1980 to 2021 are considered: (1) the ECMWF Reanalysis version 5 (ERA5) (Hersbach et al., 2020), whose spatial resolution is $0.25° \times 0.25°$; (2) the Japanese 55-year Reanalysis (JRA55) (Kobayashi et al., 2015) provided on a $1.25° \times 1.25°$ grid; and (3) the Modern-Era Retrospective analysis for Research and Applications, Version 2 (MERRA-2) (Gelaro et al., 2017) at $0.5° \times 0.625°$ spatial resolution.

Climate simulations performed with 11 different models from CMIP6 database (Eyring et al., 2016) are used. All these experiments are detailed in (Table 1). We consider only the models providing the daily mean outputs for atmospheric fields necessary to compute CAT indices (see Section 3). Two CMIP6 experiments are used: 1) the historical experiment, consisting in a climate reconstruction from the 1850-2014 period; and 2) the future projections performed under the scenario ssp5-8.5 from the Tier 1 of the Scenario Model Intercomparison Project (ScenarioMIP) (O'Neill et al., 2016). The ssp5-8.5 scenario induces the largest radiative forcing, i.e. the global warming, on the earth surface by the end of the twenty-first century. All the model data are used for the period 1970-2100.

For each experiment in 1) and 2), all the available ensemble members from the 11 coupled models are used. As the number of members is different from one model to another, we compute first the ensemble mean for a given model before computing the multi-model mean (MMM), assuring the same weighting in the MMM. In addition, a large ensemble member of 20 historical and SSP5-8.5 simulations was performed with CNRM-CM6-1 model to better estimate the signal-to-noise ratio in past and future CAT changes. All data from reanalyses and climate models were interpolated on a common $1° \times 1°$ grid before computing CAT diagnostics. A conservative remapping method was used for fields with a spatial resolution lower than 1°, whereas bilinear interpolation was applied for the rest.

3 Methods

3.1 Choice of CAT diagnostics

We focus on CAT produced by vertical wind shear and frontogenesis in upper tropospheric levels, where the core of the jet stream is located. Then, the Turbulence

Index 1 (hereinafter TI1) defined by Ellrod and Knapp (1992) and its two components, Vertical Wind Shear (VWS) and Flow deformation (DEF), are used here as CAT diagnostics. We made this choice as TI1 has shown significant skill to predict CAT encounters (Gill, 2014; Sharman et al., 2006). In particular, the probability of detection indicates that more than three-fourths of all CAT events are correctly detected by TI1 compared to pilots' reports (Ellrod & Knapp, 1992). Note that TI1 is widely used in many forecast weather centres (e.g. Météo-France, KNMI). The two World Area Forecast Centres (WAFC; London and Washington) also use TI1 as a single diagnostic to provide a global turbulence forecast on a $1.25° \times 1.25°$ grid (Gill, 2014; Kim et al., 2018; Storer et al., 2020), and TI1 is currently implemented in the graphical turbulence guidance algorithm (Sharman et al., 2006).

Following Ellrod and Knapp (1992), TI1 index is defined as the product of VWS and DEF:

$$TI1 = VWS \times DEF. \tag{1}$$

VWS is the wind field difference in the atmospheric layer:

$$VWS = \left((\frac{\partial u}{\partial z})^2 + (\frac{\partial v}{\partial z})^2 \right)^{\frac{1}{2}}, \tag{2}$$

where u is the horizontal wind velocity in the east–west direction, and v is the horizontal wind velocity in the north–south direction. The altitude z corresponding to the pressure level at each grid point is calculated by using the geopotential height. In addition, DEF combines Shearing Deformation (D_{SH}) and Stretching Deformation (D_{ST}):

$$DEF = \left(D_{SH}^2 + D_{ST}^2 \right)^{\frac{1}{2}} = \left((\frac{\partial v}{\partial x} + \frac{\partial u}{\partial y})^2 + (\frac{\partial u}{\partial x} - \frac{\partial v}{\partial y})^2 \right)^{\frac{1}{2}}. \tag{3}$$

DEF is computed at the top (200 hPa) and at the bottom (250 hPa) of the atmospheric layer. Then the resulting mean is taken as the total flow deformation in the layer (same method as in Overeem (2002)).

We select the atmospheric layer located between 200 and 250 hPa, which contains typical cruising altitudes of 10-12 km approximately. The winter season, defined here as December-January-February (DJF), is considered because this is the season where the frequency of CAT is higher in the Northern Hemisphere (Jaeger & Sprenger, 2007; J. H. Lee et al., 2023).

In order to assess the robustness of the results to the choice of CAT diagnostics, other CAT indices are used (see Section 4.4). These indices are: the negative Richardson number (- Ri), frontogenesis function, horizontal temperature gradient and the North Carolina State University index 1 (NCSU1). These indices were calculated at the same levels as those mentioned above.

3.2 Definition of the MOG-CAT category

To characterize MOG-CAT category, we followed the approach described in previous studies (J. H. Lee et al., 2023; Storer et al., 2017; P. D. Williams, 2017). This consists of defining a threshold value for a large commercial aircraft by calculating a percentile range from the probability density function of the CAT diagnostic. However, in the literature, there is no consensus on the choice of this threshold value. P. D. Williams (2017) and Storer et al. (2017) applied the 99.6th percentile as MOG-CAT threshold. This means that in the high atmosphere the probability of MOG-CAT occurrence is set to 0.4%. J. H. Lee et al. (2023) considered 5% as the probability of MOG-CAT occurrence (95th percentile), while based on pilots' reports, Sharman et al. (2006) found that the probability of upper-levels MOG-CAT is at most 1%.

In this study, we chose to apply the threshold value of 1% for MOG-CAT occurrence. This choice is also motivated by the fact that 1% also offers a larger sample size for a robust statistical treatment. Accordingly, the threshold of MOG-CAT is defined for each dataset by computing the 99th percentile from the probability density function of winter daily values over the reference period 1981-2010. Only midlatitude areas are considered, defined here as the 20-60°N latitudinal band (J. H. Lee et al., 2023).

It is worth mentioning that the spatial distribution of CAT frequency and its trends are weakly sensitive to the threshold used (not shown). We define MOG-CAT frequency at each grid point as the percentage of the values exceeding the threshold value. Note that the value of the threshold is very dependent on the horizontal resolution of the data used: the finer the resolution, the higher the threshold value. This is the reason why all the variables from the reanalyses and climate models were interpolated on a common grid before computing CAT diagnostics (see Section 2).

4 Results

4.1 MOG-CAT climatology in reanalysis and CMIP6 climate models

High frequencies of MOG-CAT occurrence are found over different regions in the Northern Hemisphere (Figure 1a): the North Atlantic, North Pacific, East-Asia and North Africa. This is consistent with previous studies, which have computed MOG-CAT climatology from other reanalysis and over different periods (Jaeger & Sprenger, 2007; J. H. Lee et al., 2023). In general, MOG-CAT occurs in the vicinity of jet-streams and the highest frequencies are located on the northern side of the jet. Very similar spatial patterns of MOG-CAT climatology are obtained from JRA55 and MERRA-2 reanalyses (not shown).

The maximum MOG-CAT frequency is located over East-Asia and can reach more than 7.0%. This is mainly due to strong VWS (Figure 1b), where the subtropical jet reaches its maximum speed. This is also due to the presence of the Himalayan mountain range that could enhance VWS. Other areas of large MOG-CAT occurrence are observed at the subtropical jet entrance, which is located over western North Africa. Here, the highest frequencies in MOG-CAT are induced by large DEF due to the presence of the Azores high (Figure 1c). It has been shown that regions of sharply curved anticyclonic flows most frequently produce CAT (Ellrod et al., 2015; Jaeger & Sprenger, 2007). Over North Pacific and northern North Atlantic areas, both VWS and DEF contribute to MOG-CAT generation (Figure 1a-c). MOG-CAT frequency peaks over high mountain chains (Himalayas, Rocky Mountains and Alps). Whereas the regridding of ERA5 onto a coarser grid does not significantly affect the spatial structure of TI1 index, the MOG-CAT characteristics over the mountainous areas are greatly affected by the interpolation for the frontogenesis function CAT diagnostic (Figure 2). This is probably due to the high resolution, which allows to better resolve the mesoscale mountain waves. However, there is no dependence on spatial resolution for MOG-CAT produced by vertical wind shear within jet-streams and upper-level fronts (Figure 2).

MOG-CAT climatology is well represented in CMIP6 models with respect to ERA5 which is considered as the reference here (Figure 3). The spatial structure of MOG-CAT occurring in the vicinity of the subtropical jet is in general well simulated in all models, although some of these models overestimate MOG-CAT frequency over East-Asia and North Pacific (MIROC-ES2L, UKESM1-0-LL) and others underestimate it (CNRM-CM6-1, CanESM5, MPI-ESM1-2-HR). Over the North Atlantic, most of the models underestimate MOG-CAT frequency except CNRM-CM6-1 and EC-Earth3, which represent better the spatial distribution of MOG-CAT. In general, over the North Atlantic, models simulate higher MOG-CAT frequency at lower latitudes, over the subtropical jet entrance. This is partly due to the fact that CMIP6 models feature a stronger VWS over the subtropical jet than over the polar jet with respect to ERA5

(Figure 4). Focusing on the MMM, MOG-CAT frequencies over East-Asia, North Africa and North Pacific are close to ERA5 (Figure 3). However, over the North Atlantic area, MMM MOG-CAT frequency is approximately twice weaker than in ERA5, pointing out that CMIP6 models display some deficiencies in simulating CAT extremes in this area.

4.2 MOG-CAT past trends

We define a common period, 1980-2021, to investigate past trends in MOG-CAT frequency. For this purpose, we compute at each grid point the trend (signal) of the interannual time series of winter MOG-CAT frequency by using a linear least-squares regression method. Then, the trend value is normalised by the interannual standard deviation (noise) of the time series. We proceed in this way to assess if the trend is larger than the interannual variability of MOG-CAT in winter. Note that to generate robust statistics, only the grid points showing a sufficient number of MOG-CAT episodes during the period of study were taken into account in the trend estimation. We selected the grids points with more than 50% values different from zero in the time-series, i.e. the grid points with more than 21 winters of non-zero MOG-CAT values. We proceed in the same way to assess VWS and DEF trends.

Figure 5a shows that for ERA5, the largest positive values of the signal-to-noise ratio are observed in several regions: East Asia, Middle East, North Pacific and North Atlantic. The increase in MOG-CAT frequency over the last decades in these different regions is associated with a large increase in VWS (Figure 5b) over the jet streams. VWS near jet-streams is highly correlated with the meridional temperature gradient according to the thermal wind balance. This suggests that the increase in VWS could be related to the positive trends in the meridional temperature gradient in the upper levels, which are likely due to the tropical upper-tropospheric warming and the polar lower-stratospheric cooling during the recent decades (J. H. Lee et al., 2023). Over the North Atlantic, the positive trends in MOG-CAT are driven by both VWS and DEF (Figure 5b and 5c).

We assess MOG-CAT trends obtained with other reanalyses over the four regions indicated with the boxes in Figure 5. In the North Atlantic, we consider two domains: (i) North Atlantic polar-jet exit; and (ii) Southern North Atlantic subtropical-jet entrance. This splitting allows to separate CAT produced by the polar jet from that produced by the subtropical jet. The polar jet stream is often described as eddy-driven and is distinct from the subtropical jet stream, which is primarily caused by poleward transport of angular momentum in the Hadley cell (S. H. Lee et al., 2019). The other two domains are: (iii) North Pacific, where the two polar and subtropical jets merge; and (iv) Middle-East and East-Asia, where CAT is mainly produced by the subtropical-jet and strengthened by the Himalayas. These regions have been selected because large positive trends are observed in recent decades (Figure 5). Besides, these regions are characterised by a high density of air traffic linking Europe, North America, East Asia and Middle-East.

For each region, the winter annual MOG-CAT frequency is defined by computing the percentage of the values that exceeds MOG-CAT threshold relative to the total number of values (number of grid points $\times$ number of winter days of each year). Then, the percentages of change shown in (Table 2) are obtained using the total change for the whole period (slope of the trend line $\times$ 42 years) compared to the frequency in 1980 of the fitted linear trend lines.

ERA5, JRA55 and MERRA-2 are in good agreement with the increase of MOG-CAT over the four regions (Table 2). A mean percentage of change of 61.8% was obtained over northern North Atlantic for MOG-CAT and 155.9% over southern North Atlantic. Over the North Pacific MOG-CAT increases by 61.1%, and over East Asia and Middle East by 106% on average. Note that the values of the increases are much higher with JRA55 compared to ERA5 and MERRA-2 over southern North Atlantic, East Asia and Middle

East. The trends are generally robust and statistically significant at 1% level (p-value $<$ 0.01), except over the northern North Atlantic. The largest increases of MOG-CAT are found over Northwestern Africa, East Asia and Middle East, where MOG-CAT frequency has more than doubled between 1980 and 2021, mainly due to a sharp increase in VWS.

Next step is to investigate the possible causes of these MOG-CAT increases. To analyse the respective role of internal versus externally forced variability, we use the historical experiments performed by CMIP6 models (Table 1). The multi-model multi-member ensemble allows to isolate the forced climate response from the internal climate variability. The externally forced component of the simulated MOG-CAT trends can be obtained by averaging the trends from all the members together (Deser et al., 2014, 2016).

Figure 6 compares the observed MOG-CAT trends in ERA5 with the forced MOG-CAT trends in CMIP6 models. Like the observed trend pattern, the forced response shows some evidence for the increase of MOG-CAT frequency over East Asia, Middle East and North Africa. This indicates that the MOG-CAT response to global warming is strong enough to be detected over these regions, pointing out the potential influence of human-induced climate factors on these trends. Over the North Atlantic and the North Pacific, there is no agreement between the observed MOG-CAT trend and the forced response, suggesting that the internal climate variability is still very large with respect to the GHGs effect in these regions. Overall, the values of the observed MOG-CAT trends lie within the range of simulated predictions, except over the northern North Atlantic and North America (Figure 6).

In complement, we also used only the 20 members of the CNRM-CM6.1 model to isolate the effects of anthropogenic climate change from those of internal variability on MOG-CAT trends. A forced response similar in pattern to that of the multi-model ensemble members was obtained (Figure 7a). In addition, here we provide a quantitative assessment using a simple signal-to-noise analysis. The signal is obtained by averaging across the 20 members of the CNRM-CM6.1 model, and the noise is the spread amongst all the members (Deser et al., 2014, 2016). High positive values of the signal-to-noise ratio are found over East Asia, Middle East and North Africa (Figure 7b), indicating that the changes in MOG-CAT frequency could be attributed to a response of the atmosphere to external forcings (i.e. GHG increases) over these regions. In contrast, over the North Atlantic and the North Pacific, the signal-to-noise ratio is very weak, suggesting that the amplitude of internal variability in recent decades is still very strong to make the global warming signals detectable. Over the North Atlantic, the individual ensemble members reveal a wide range of MOG-CAT trend responses to the same external forcing. For example, members 15 and 16 exhibit opposite sign (Figure 7c and 7d). Our findings are in agreement with the study by Tenenbaum et al. (2022), which used 20 years of aircraft observations of the New York to London flights over North Atlantic and which reported that the turbulence trends are not statistically significant. Our findings are also consistent with the study by J. H. Lee et al. (2023), in which the largest positive MOG-CAT trends were found in East Asia between 1979 and 2019.

4.3 MOG-CAT future changes

We investigate MOG-CAT changes in the future climate projections by considering different global warming levels (GWLs) rather than the time horizon. For this purpose, we apply the epoch approach, also called the time-shift method, used in the International Panel on Climate Change (IPCC) AR6 report (see section 4.6.1 in Masson-Delmotte et al. (2021)). As mentioned in the IPCC AR6, this method offers significant advantages compared to the widely-used time horizon approach, since it allows future projections to be combined independently from the emissions scenarios and the climate sensitivity in coupled models. Moreover, the use of GWLs to assess changes in extreme events is more meaningful for decision makers as actionable information is provided (IPCC AR6,

chapter 11). The method consists of setting different GWL levels (1°C, 2°C, 3°C, 4°C) with respect to the 1850–1900 period. Here we define the reference as GWL = 1°C , which in fact corresponds to the GWL currently observed (∼1.1°C). We consider three different future climates at GWLs = 2°C, 3°C, 4°C. We first proceed by computing 20-year moving averages of the global average surface temperature for each member of each model. Note that the year in which a GWL is exceeded is different across the different simulations. Then we examine when the required GWL is reached with respect to our reference GWL. Once the year in which the GWL was exceeded is obtained, a 20-year period centred on this year is computed. This 20-year period is used to be representative of the required GWL and composites for other variables can be obtained by using this period. Finally, for each member of each model, MOG-CAT frequency is calculated for the present GWL = 1°C and for each future GWL=2°C, 3°C, 4°C and the respective differences are computed. We note here ΔT the global mean temperature difference between each future GWL and the present GWL.

Large increases in MOG-CAT frequency are projected over most regions within the latitudinal band 20-40°N, located over East Asia, Middle East, North Africa, North Pacific and North America (Figure 8). Moreover, there is generally a high model agreement about this increase. These projected changes in MOG-CAT frequency are enhanced as the GWL increases. However, at higher latitudes the values of the projected changes obtained by the MMM are small with low model agreement, in particular over the North Atlantic. However, these uncertainties are much reduced for ΔT=2°C and 3°C, for which the MMM projects a reduction of the MOG-CAT in the future (Figure 8b and 8c).

We use the large ensemble of CNRM-CM6.1 model to investigate the role of the internal variability on the different GWL projections. This is measured as the agreement amongst the 20 members of the ensemble (Figure 9). The effects of internal variability on the MOG-CAT frequency are moderate for ΔT =1°C, but very weak for larger GWLs, since a high member agreement is obtained. As expected, the response of external forcing (GHGs) becomes dominant as GWL increases. CNRM-CM6.1 projections are similar to the MMM response shown in Figure 8, indicating the appropriateness of using large ensembles (Deser et al., 2014, 2012; Kay et al., 2015).

Figure 10 suggests that the projected changes in MOG-CAT frequency shown in Figure 8 are mostly caused by the increase in VWS within the subtropical jet (20-40°N latitudinal band). According to the thermal wind balance relation, the increase of VWS in the last four decades is highly correlated with the strengthening of the meridional temperature gradient (J. H. Lee et al., 2023). Our results would support that the meridional temperature gradient is likely projected to be reinforced in the future climate as a response to anthropogenic climate change, leading to stronger subtropical jet and an increase in VWS. Despite the increase in DEF over the North Atlantic, the combination with VWS shows a weak decrease in MOG-CAT (Figure 10).

It is worth noting that we find no impact of the model horizontal resolution on the results. Indeed, the ensemble of CMIP6 models used in this study includes two high-resolution models. We found no differences in the results on the original and interpolated grids (not shown). Further, by comparing ERA5 in the native grid (∼25 km) and interpolated grid (∼100 km), we found very similar results in MOG-CAT climatology and trends (Figure 2). This is consistent with the study by Smith et al. (2023): they used three different models with high and coarse resolutions for each one, and they found no dependence on model resolution for moderate CAT projections over the North Atlantic.

4.4 Extension to other CAT indices

An extension of the analysis to other CAT indices is carried out to assess the uncertainty associated with the different CAT diagnostics. We select an ensemble of 5 CAT diagnostics, whose predictive skill to characterize CAT has been demonstrated and

validated with observational data (P. D. Williams & Storer, 2022; Sharman et al., 2006). Besides TI1 index, the new diagnostics include: frontogenesis function, horizontal temperature gradient, - Ri, and NCSU1. They are described in detail by Sharman et al. (2006). These indices are currently implemented in the graphical turbulence guidance algorithm. Sharman et al. (2006) showed that these diagnostics perform best in forecasting upper-level turbulence phenomena. Using this subset therefore ensures that the results are as robust as possible. Note that our approach differs from previous studies, which use a large number of turbulence diagnostics (P. D. Williams, 2017; Storer et al., 2017; Smith et al., 2023); most of these diagnostics are important ingredients in CAT production but cannot be considered as CAT indices when used alone.

The spatial patterns of projected changes in MOG-CAT frequency for ΔT=2°C are similar among the CAT diagnostics (Figure 11). Large increases in MOG-CAT frequency are obtained over different regions in the latitudinal band 20-40°N (East Asia, Middle East, North Africa, North Pacific and North America). Note that the frontogenesis function presents weaker changes compared to the other indices but they are located in the same areas. Figure 11 shows that over East Asia, Middle East, North Africa, North Pacific and North America, the multi-diagnostic multi-model mean is quite in agreement on an increase in MOG-CAT frequency as a consequence of global warming. The largest increases in MOG-CAT frequency are projected to occur over East Asia.

Again, over the North Atlantic, the projected changes are weak and there is less agreement amongst the CAT diagnostics. The sign of the change is negative for three out of the five indices used (TI1, horizontal temperature gradient, frontogenesis function) and positive for - Ri and NCSU1, which takes into account Ri in its computation. Ri is defined as the ratio between the squared Brunt-Väisälä frequency N^2 (which is related to static instability) and the squared VWS. This indicates that projected increase in MOG-CAT frequency shown by Ri over the North Atlantic is mostly explained by the increases in the static instability rather than by VWS, which is projected to decrease over this area (Figure 11). Indeed, the use of Ri to characterize CAT could be misleading, since the static instability, although a turbulence measure, can also be related to convective turbulence which is visible. The climatology of Ri shows that the highest frequencies are located over the tropics, which are well known to be regions of convective turbulence (not shown). Another limitation of using Ri is that this index is more reliable when estimated from high-resolution data (Ellrod et al., 2015).

Our results suggest that the uncertainty in MOG-CAT projections over North Atlantic between CAT indices is related to the competition between changes in the wind shear and convective instability phenomena, both sources of turbulence. It is important to recall that wind shear instability is the most important ingredient in CAT generation (Dutton & Panofsky, 1970; Ellrod et al., 2015; Sharman & Lane, 2016). This uncertainty linked to CAT diagnostics implies that the CAT phenomenon is complex and that all the phenomena that generate it should be studied in order to understand future changes.

The disagreement in CAT projections amongst twenty diagnostics can also be found in Figure 2 of Storer et al. (2017) based on the HadGEM2-ES model. Over the North Atlantic, the TI1 index shows a weak decrease. In contrast, DEF increases considerably (up to 500%), which is consistent with our results (Figure 11). More recently, Smith et al. (2023) found that over the North Atlantic, twelve diagnostics projected a moderate CAT increase, while six projected a decrease. Furthermore, P. D. Williams and Storer (2022) showed a strong inter-diagnostic uncertainty in CAT climatology and trends with ERA-interim reanalysis and HadGEM2-ES model. Thus, while it is crucial to study CAT changes from a multi-diagnostic approach, averaging across all diagnostics may complicate interpretation of results since the diagnostics can represent very different physical phenomena.

5 Conclusions and Discussion

This study provides an assessment of past and future changes in MOG-CAT frequency over the Northern Hemisphere by using different atmospheric reanalyses and experiments performed with 11 CMIP6 climate models.

Consistently with previous studies (Jaeger & Sprenger, 2007; J. H. Lee et al., 2023), we find that highest frequencies of MOG-CAT occurrence in the current climate are located on the northern side of the jets over different regions: the North Atlantic, North Pacific, East-Asia and North Africa. The maxima of MOG-CAT frequency were found over East-Asia (approximately 7.5%), which are due to strong vertical wind shear (VWS) where subtropical jet reaches its speed maximum, and which are also due to the presence of the Himalayas that could enhance VWS. In addition, this study performs the first validation of CMIP6 models in terms of simulated MOG-CAT climatology with different CAT diagnostics. We conclude that these models are suitable tools to study MOG-CAT. Nevertheless, we show that over the North Atlantic region, most models underestimate MOG-CAT frequency, mainly due to the fact that CMIP6 models simulate weaker vertical wind shear within the polar jet with respect to ERA5 reanalysis (Figure 4).

Past changes in MOG-CAT frequency for the period 1980-2021 show increases in East Asia, Middle East, North Africa and North Pacific. The different atmospheric reanalyses are in good agreement and the trends are statistically significant at 1% level. Over the North Atlantic, the reanalyses show positive trends that are not statistically significant. We find that in recent decades, frequency of MOG-CAT has more than doubled over Northwestern Africa, Middle East, and Eastern Asia. This is mainly due to a large increase in VWS related to the subtropical jet strengthening, which is due in turn to the sharpening of the meridional temperature gradient caused by the warming over the tropics and the cooling over high latitudes in upper atmospheric levels. The importance of the internal climate variability with regards to the anthropogenic forcing is addressed by using CMIP6 models and a large ensemble performed with the CNRM-CM6.1 model. We find that over the North Pacific and the North Atlantic regions, the internal climate variability is large enough to mask the anthropogenic-induced signal. In addition, the increase in MOG-CAT frequency observed in East Asia and Middle East over the last four decades is outside the range of internal variability and could be potentially attributed to external forcing.

Multi-model climate projections indicate that the positive trend reported over North Africa, East Asia and Middle East will continue to increase in the future with the global warming level, and there is a high agreement amongst the climate models and the CAT diagnostics. In general, models project a MOG-CAT increase within the 20-40°N latitudinal band and a weak decrease northwards. The projected increases in MOG-CAT frequency over these regions intensify with the degree of global surface warming considered. Component analysis of the TI1 CAT index leads to the conclusion that increases in MOG-CAT frequency are mainly related to increases in VWS within the subtropical jet. Contrary to previous studies (P. D. Williams, 2017; Storer et al., 2017; Smith et al., 2023), our results show a slight decrease in MOG-CAT frequency over the North Atlantic. The disagreement over this region can be explained by the fact that there are large uncertainties associated with the CAT indices used. We suggest that this uncertainty may be linked to competition between vertical wind shear and convective instability, both sources of turbulence. However, it is important to recall that shear instability is the main source of clear-air turbulence, and that vertical wind shear is projected to decrease over the North Atlantic.

The projected increases in MOG-CAT frequency shown in this study could have a significant impact on aviation operations and safety, as well as on the design of future aircrafts. Future work is needed to extend the analysis to other atmospheric layers (e.g., 150-200 hPa, 250-300 hPa). This is of interest since future commercial aircraft could be

optimised to fly at other altitudes to mitigate the projected increase in MOG-CAT frequency found at the current cruising altitudes. Furthermore, in-flight turbulence data could be used to study the reliability of CAT indices. In particular over the North Atlantic, this would provide a better understanding of CAT generation mechanisms and reduce MOG-CAT projection uncertainties. Collaborations with government agencies regulators of civil aviation and airlines are necessary to have access to these in-flight measurements.

Future research is also needed to investigate future changes in CAT intensity together with wind gust to define the maximum load an aircraft can withstand. To study properly the impact of CAT extreme intensities on a commercial aircraft, spatial scales ranging from 100 m to 2 km are suitable. The use of dynamical downscaling approaches, in which a regional model is nested by a coarser resolution global model, could be of interest to address future changes in CAT intensity over a certain region.

Open Research

The ERA5 reanalysis on pressure levels can be downloaded here: https://cds.climate.copernicus.eu/cdsapp#!/dataset/reanalysis-era5-pressure-levels?tab=form, JRA55 were obtained from: https://rda.ucar.edu/datasets/ds628.0/index.html#!access, and MERRA-2 can be downloaded from: https://disc.gsfc.nasa.gov/datasets?project=MERRA-2. All CMIP6 data analyzed in this study were obtained from the Institut Pierre Simon Laplace (IPSL) node of the Earth System Grid Federation (ESGF): https://esgf-node.ipsl.upmc.fr/search/cmip6-ipsl/. The 20 simulations performed with CNRM-CM6-1 model can be provided by the authors upon request.

Acknowledgments

The authors thanks the climate modeling groups for producing the CMIP6 data and the Earth System Grid Federation (ESGF) for archiving the data and providing access freely available. We gratefully thank Marie-Pierre Moine and Laure Coquart for their help to handle the CNRM-CM6-1 climate model. The authors thank the CNRM-CERFACS modeling group for developing and supporting the CNRM-CM6-1 model. We thank P. D. Williams for valuable comments on this work, for the helpful discussions and for hosting M. Foudad at the University of Reading in June 2023, we would also aknowledge Didier Ricard from Météo-France/CNRM and Marc Wetterwald from Airbus for helpful discussions.

References

Boucher, O., Servonnat, J., Albright, A. L., Aumont, O., Balkanski, Y., Bastrikov, V., ... others (2020). Presentation and evaluation of the IPSL-CM6A-LR climate model. *Journal of Advances in Modeling Earth Systems*, *12*(7), e2019MS002010. doi: https://doi.org/10.1029/2019MS002010

Deser, C., Phillips, A. S., Alexander, M. A., & V, S. B. (2014). Projecting North American climate over the next 50 years: uncertainty due to internal variability. *Journal of Climate*, *27*(6), 2271–2296. doi: https://doi.org/10.1175/JCLI-D-13-00451.1

Deser, C., Phillips, A. S., Bourdette, V., & Teng, H. (2012). Uncertainty in climate change projections: the role of internal variability. *Climate Dynamics*, *38*, 527–546. doi: https://doi.org/10.1007/s00382-010-0977-x

Deser, C., Terray, L., & Phillips, A. S. (2016). Forced and internal components of winter air temperature trends over north america during the past 50 years: Mechanisms and implications. *Journal of Climate*, *29*(6), 2237–2258. doi:

http://dx.doi.org/10.1175/JCLI-D-15-0304.s1

Döscher, R., Acosta, M., Alessandri, A., Anthoni, P., Arneth, A., Arsouze, T., ... others (2021). The EC-Earth3 Earth system model for the Coupled Model Intercomparison Project 6. *Geoscientific Model Development Discussions*, *2021*, 1–90. doi: https://doi.org/10.5194/gmd-15-2973-2022

Dutton, J. A., & Panofsky, H. A. (1970). Clear air turbulence: A mystery may be unfolding: High altitude turbulence poses serious problems for aviation and atmospheric science. *Science*, *167*(3920), 937–944. doi: https://doi.org/10.1126/science.167.3920.937

Ellrod, G. P., & Knapp, D. I. (1992). An objective clear-air turbulence forecasting technique: Verification and operational use. *Weather and Forecasting*, *7*(1), 150–165. doi: https://doi.org/10.1175/1520-0434(1992)007%3C0150:AOCATF%3E2.0.CO;2

Ellrod, G. P., Knox, J. A., Lester, P. F., & Ehernberger, L. J. (2015). Clear air turbulence. In G. R. North, J. Pyle, & F. Zhang (Eds.), *Encyclopedia of atmospheric science, 2nd edn* (pp. 177–186). Elsevier. doi: https://doi.org/10.1016/B978-0-12-382225-3.00104-3

Eyring, V., Bony, S., Meehl, G. A., A, S. C., Stevens, B., Stouffer, R. J., & Taylor, K. E. (2016). Overview of the Coupled Model Intercomparison Project Phase 6 (CMIP6) experimental design and organization. *Geoscientific Model Development*, *9*(5), 1937–1958. doi: https://doi.org/10.5194/gmd-9-1937-2016

Gelaro, R., McCarty, W., Suárez, M. J., Todling, R., Molod, A., Takacs, L., ... Zhao, B. (2017). The Modern-Era Retrospective Analysis for Research and Applications, Version 2 (MERRA-2). *Journal of Climate*, *30*(14), 5419–5454. doi: https://doi.org/10.1175/JCLI-D-16-0758.1

Gill, P. G. (2014). Objective verification of World Area Forecast Centre clear air turbulence forecasts. *Meteorological Applications*, *21*(1), 3–11. doi: https://doi.org/10.1002/met.1288

Gultepe, I., Sharman, R., Williams, P., Zhou, B., Ellrod, G., Minnis, P., ... Neto, F. (2019). A review of high impact weather for aviation meteorology. *Pure and Applied Geophysics*, *176*, 1869–1921. doi: https://doi.org/10.1007/s00024-019-02168-6

Hajima, T., Watanabe, M., Yamamoto, A., Tatebe, H., Noguchi, M. A., Abe, M., ... others (2020). Development of the MIROC-ES2L Earth system model and the evaluation of biogeochemical processes and feedbacks. *Geoscientific Model Development*, *13*(5), 2197–2244. doi: https://doi.org/10.5194/gmd-13-2197-2020

Hawkins, E., & Sutton, R. (2011). The potential to narrow uncertainty in projections of regional precipitation change. *Climate dynamics*, *37*, 407–418. doi: https://doi.org/10.1007/s00382-010-0810-6

Hersbach, H., Bell, B., P., B., Hirahara, S., Horányi, A., Muñoz-Sabater, J., ... Thépaut, J. (2020). The ERA5 global reanalysis. *Quarterly Journal of the Royal Meteorological Society*, *146*(730), 1999–2049. doi: https://doi.org/10.1002/qj.3803

Jaeger, E. B., & Sprenger, M. (2007). A Northern Hemispheric climatology of indices for clear air turbulence in the tropopause region derived from ERA40 reanalysis data. *Journal of Geophysical Research: Atmospheres*, *112*(D20). doi: https://doi.org/10.1029/2006JD008189

Kay, J. E., Deser, C., Phillips, A., Mai, A., Hannay, C., Strand, G., ... Vertenstein, M. (2015). The Community Earth System Model (CESM) large ensemble project: A community resource for studying climate change in the presence of internal climate variability. *Bulletin of the American Meteorological Society*, *96*(8), 1333–1349. doi: https://doi.org/10.1175/BAMS-D-13-00255.1

Kim, J.-H., Sharman, R., Strahan, M., Scheck, J. W., Bartholomew, C., Cheung, J. C., ... Gait, N. (2018). Improvements in nonconvective aviation turbulence prediction for the world area forecast system. *Bulletin of the American Meteorological Society*, *99*(11), 2295–2311. doi: https://doi.org/10.1175/BAMS-D-17-0117.1

Kobayashi, S., Ota, Y., Harada, Y., Ebita, A., Moriya, M., Onoda, H., ... others (2015).

The JRA-55 reanalysis: General specifications and basic characteristics. *Journal of the Meteorological Society of Japan. Ser. II*, *93*(1), 5–48. doi: https://doi.org/10.2151/jmsj.2015-001

Lee, J. H., Kim, J.-H., Sharman, R. D., Kim, J., & Son, S.-W. (2023). Climatology of clear-air turbulence in upper troposphere and lower stratosphere in the Northern Hemisphere using ERA5 reanalysis data. *Journal of Geophysical Research: Atmospheres*, *128*(1), e2022JD037679. doi: https://doi.org/10.1029/2022jd037679

Lee, S. H., Williams, P. D., & Frame, T. H. (2019). Increased shear in the North Atlantic upper-level jet stream over the past four decades. *Nature*, *572*(7771), 639–642. doi: https://doi.org/10.1038/s41586-019-1465-z

Lv, Y., Guo, J., Li, J., Han, Y., Xu, H., Guo, X., ... Gao, W. (2021). Increased Turbulence in the Eurasian upper-level jet stream in winter: Past and future. *Earth and Space Science*, *8*(2), e2020EA001556. doi: https://doi.org/10.1029/2020EA001556

Masson-Delmotte, V., Zhai, P., Pirani, A., Connors, S. L., Péan, C., Berger, S., ... Zhou, B. (2021). *IPCC: Climate Change 2021 – The Physical Science Basis: Working Group I Contribution to the Sixth Assessment Report of the Intergovernmental Panel on Climate Change*. Cambridge, United Kingdom and New York, NY, USA: Cambridge University Press. doi: https://doi.org/10.1017/9781009157896

Müller, W. A., Jungclaus, J. H., Mauritsen, T., Baehr, J., Bittner, M., Budich, R., ... others (2018). A high-resolution version of the Max Planck Institute Earth System Model (MPI-ESM1. 2-HR). *Journal of Advances in Modeling Earth Systems*, *10*(7), 1383–1413. doi: https://doi.org/10.1029/2017MS001217

O'Neill, B. C., Tebaldi, C., Van Vuuren, D. P., Eyring, V., Friedlingstein, P., Hurtt, G., ... others (2016). The Scenario Model Intercomparison Project (ScenarioMIP) for CMIP6. *Geoscientific Model Development*, *9*(9), 3461–3482. doi: https://doi.org/10.5194/gmd-9-3461-2016

Overeem, A. (2002). *Verification of clear-air turbulence forecasts* (Tech. Rep.). KNMI (Royal Netherlands Meteorological Institute).

Seland, Ø., Bentsen, M., Olivié, D., Toniazzo, T., Gjermundsen, A., Graff, L. S., ... others (2020). Overview of the Norwegian Earth System Model (NorESM2) and key climate response of CMIP6 DECK, historical, and scenario simulations. *Geoscientific Model Development*, *13*(12), 6165–6200. doi: https://doi.org/10.5194/gmd-13-6165-2020

Sellar, A. A., Jones, C. G., Mulcahy, J. P., Tang, Y., Yool, A., Wiltshire, A., ... others (2019). UKESM1: Description and evaluation of the UK Earth System Model. *Journal of Advances in Modeling Earth Systems*, *11*(12), 4513–4558. doi: https://doi.org/10.1029/2019MS001739

Sharman, R., & Lane, T. (2016). *Aviation turbulence: Processes, detection, and prediction*. Berlin: Springer. doi: https://doi.org/10.1007/978-3-319-23630-8

Sharman, R., Tebaldi, C., Wiener, G., & Wolff, J. (2006). An integrated approach to mid-and upper-level turbulence forecasting. *Weather and forecasting*, *21*(3), 268–287. doi: https://doi.org/10.1175/WAF924.1

Sharman, R., Trier, S., Lane, T., & Doyle, J. (2012). Sources and dynamics of turbulence in the upper troposphere and lower stratosphere: A review. *Geophysical Research Letters*, *39*(12). doi: https://doi.org/10.1029/2012GL051996

Shaw, T., Baldwin, M., Barnes, E. A., Caballero, R., Garfinkel, C., Hwang, Y.-T., ... others (2016). Storm track processes and the opposing influences of climate change. *Nature Geoscience*, *9*(9), 656–664. doi: https://doi.org/10.1038/ngeo2783

Smith, I. H., Williams, P. D., & Schiemann, R. (2023). Clear-air turbulence trends over the North Atlantic in high-resolution climate models. *Climate Dynamics*, 1–17. doi: https://doi.org/10.1007/s00382-023-06694-x

Storer, L. N., Gill, P. G., & Williams, P. D. (2020). Multi-diagnostic multi-model ensemble forecasts of aviation turbulence. *Meteorological Applications*, *27*(1), e1885. doi: https://doi.org/10.1002/met.1885

Storer, L. N., Williams, P. D., & Gill, P. G. (2019). Aviation turbulence: dynamics, forecasting, and response to climate change. *Pure and Applied Geophysics*, *176*, 2081–2095. doi: https://doi.org/10.1007/s00024-018-1822-0

Storer, L. N., Williams, P. D., & Joshi, M. M. (2017). Global response of clear-air turbulence to climate change. *Geophysical Research Letters*, *44*(19), 9976–9984. doi: https://doi.org/10.1002/2017GL074618

Swart, N. C., Cole, J. N., Kharin, V. V., Lazare, M., Scinocca, J. F., Gillett, N. P., ... others (2019). The Canadian Earth System Model version 5 (CanESM5. 0.3). *Geoscientific Model Development*, *12*(11), 4823–4873. doi: https://doi.org/10.5194/gmd-12-4823-2019

Tatebe, H., Ogura, T., Nitta, T., Komuro, Y., Ogochi, K., Takemura, T., ... others (2019). Description and basic evaluation of simulated mean state, internal variability, and climate sensitivity in MIROC6. *Geoscientific Model Development*, *12*(7), 2727–2765. doi: https://doi.org/10.5194/gmd-12-2727-2019

Tenenbaum, J., Williams, P. D., Turp, D., Buchanan, P., Coulson, R., Gill, P. G., ... Rukhovets, L. (2022). Aircraft observations and reanalysis depictions of trends in the North Atlantic winter jet stream wind speeds and turbulence. *Quarterly Journal of the Royal Meteorological Society*, *148*(747), 2927–2941. doi: https://doi.org/10.1002/qj.4342

Uppala, S. M., Kållberg, P., Simmons, A. J., Andrae, U., Bechtold, V. D. C., Fiorino, M., ... others (2005). The ERA-40 re-analysis. *Quarterly Journal of the Royal Meteorological Society: A journal of the atmospheric sciences, applied meteorology and physical oceanography*, *131*(612), 2961–3012. doi: https://doi.org/10.1256/qj.04.176

Voldoire, A., Saint-Martin, D., Sénési, S., Decharme, B., Alias, A., Chevallier, M., ... others (2019). Evaluation of CMIP6 deck experiments with CNRM-CM6-1. *Journal of Advances in Modeling Earth Systems*, *11*(7), 2177–2213. doi: https://doi.org/10.1029/2019MS001683

Volodin, E., Mortikov, E., Kostrykin, S., Galin, V. Y., Lykossov, V., Gritsun, A., ... Iakovlev, N. (2017). Simulation of the present-day climate with the climate model INMCM5. *Climate dynamics*, *49*, 3715–3734. doi: https://doi.org/10.1007/s00382-017-3539-7

Williams, K., Copsey, D., Blockley, E., Bodas-Salcedo, A., Calvert, D., Comer, R., ... others (2018). The Met Office global coupled model 3.0 and 3.1 (GC3. 0 and GC3. 1) configurations. *Journal of Advances in Modeling Earth Systems*, *10*(2), 357–380. doi: https://doi.org/10.1002/2017MS001115

Williams, P. D. (2016). Transatlantic flight times and climate change. *Environmental Research Letters*, *11*(2), 024008. doi: http://dx.doi.org/10.1088/1748-9326/11/2/024008

Williams, P. D. (2017). Increased light, moderate, and severe clear-air turbulence in response to climate change. *Advances in Atmospheric Sciences*, *34*(5), 576–586. doi: https://doi.org/10.1007/s00376-017-6268-2

Williams, P. D., & Joshi, M. M. (2013). Intensification of winter transatlantic aviation turbulence in response to climate change. *Nature Climate Change*, *3*(7), 644–648. doi: https://doi.org/10.1038/nclimate1866

Williams, P. D., & Storer, L. N. (2022). Can a climate model successfully diagnose clear-air turbulence and its response to climate change? *Quarterly Journal of the Royal Meteorological Society*, *148*(744), 1424–1438. doi: https://doi.org/10.1002/qj.4270

Table 1. *List of CMIP6 Climate Models Used in this Study with the Experiments Used and Number of Members. The Spatial Resolution and the Reference Paper of Each Model are also Provided*

Model	Historical members	SSP5-8.5 members	Spatial resolution	reference
$CNRM-CM6-1$	20	20	$1.4° \times 1.4°$	Voldoire et al. (2019)
$IPSL-CM6A-LR$	33	7	$2.5° \times 1.3°$	Boucher et al. (2020)
$CanESM5$	10	10	$2.8° \times 2.8°$	Swart et al. (2019)
$MIROC-ES2L$	10	10	$2.8° \times 2.8°$	Hajima et al. (2020)
$UKESM1-0-LL$	5	5	$1.875° \times 1.25°$	Sellar et al. (2019)
$HadGEM3-GC31-LL$	4	4	$1.875° \times 1.25°$	K. Williams et al. (2018)
$EC-Earth3$	3	3	$0.7° \times 0.7°$	Döscher et al. (2021)
$MIROC6$	3	3	$1.4° \times 1.4°$	Tatebe et al. (2019)
$INM-CM5$	1	1	$2° \times 1.5°$	Volodin et al. (2017)
$MPI-ESM1-2-HR$	1	1	$0.9° \times 0.9°$	Müller et al. (2018)
$NorESM2-LM$	1	1	$2.5° \times 1.9°$	Seland et al. (2020)

Note. CMIP6, Coupled Model Intercomparison Project Phase 6; SSP5-8.5; Shared Socio-economic Pathway 5.

Table 2. *Percentage of Change in winter MOG-CAT Frequency for the Period 1980-2021 over the Four Regions Indicated in the Boxes in (Figure 5). The Methodology to Compute the Percentage of Change is Detailed in the Text. Bold Police Indicate Those Changes that are Significant at the 99% Level (p value < 0.01) by Using a two-tailed t test.*

Reanalysis	Northern NA			Southern NA		
	TI1	VWS	DEF	TI1	VWS	DEF
ERA5	55.4	38.4	33.3	**112.7**	**120.7**	75.2
JRA55	65.8	47.7	43.6	**197.9**	**308.7**	91.4
MERRA2	64.2	69.5	31.8	**157.3**	**151.1**	74.3

Reanalysis	North Pacific			Middle-East/East-Asia		
	TI1	VWS	DEF	TI1	VWS	DEF
ERA5	**63.1**	45.9	-8.8	**82.6**	**116.6**	59.3
JRA55	**63.2**	56.0	-1.8	**164.4**	**330.8**	**109.6**
MERRA2	**56.9**	**70.9**	-11.6	**71.0**	**84.9**	51.2

Note. MOG-CAT, Moderate-Or-Greater Clear-Air Turbulence; NA, North Atlantic; TI1, Turbulence Index 1; VWS, vertical wind shear; DEF, flow deformation.

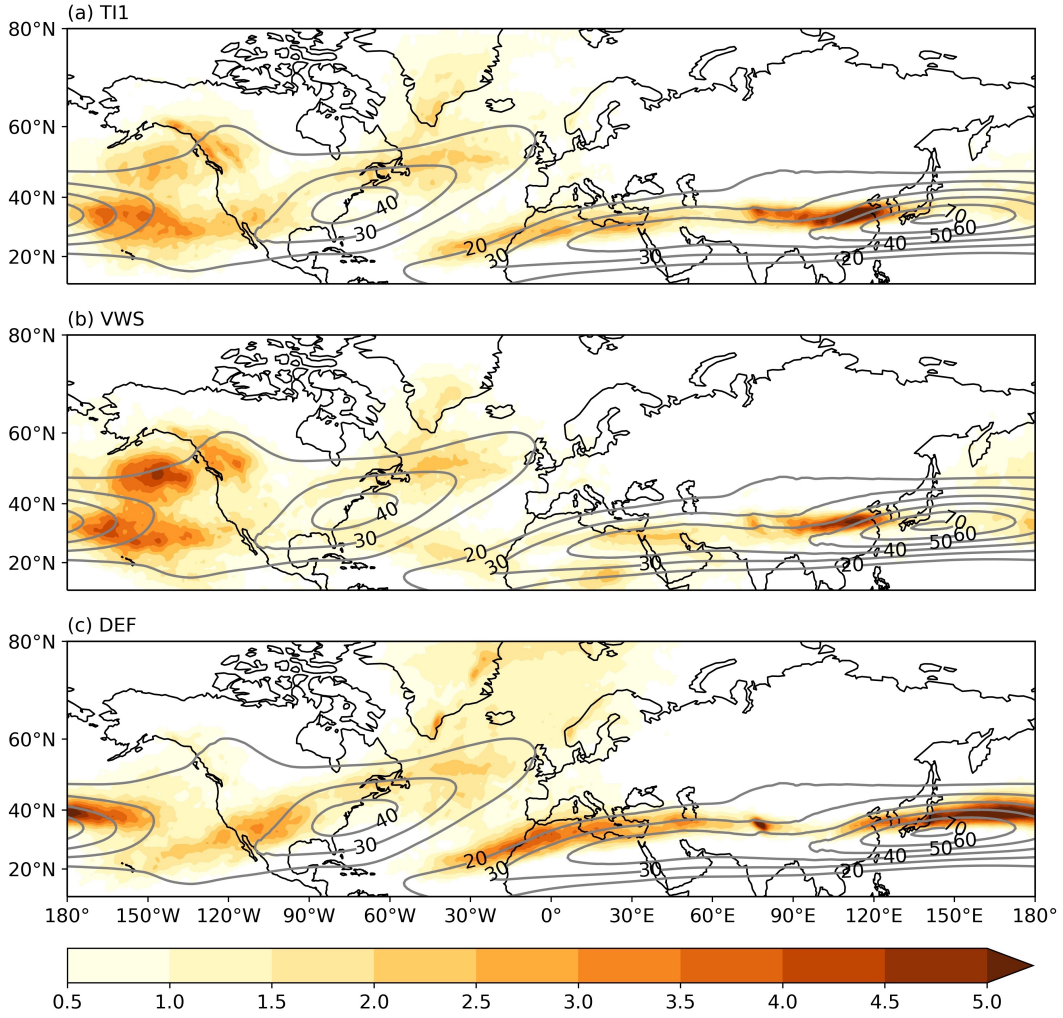

Figure 1. Winter (DJF) climatology of MOG-CAT frequency (≥ 0.5) for (a) Turbulence Index 1 (TI1), (b) Vertical Wind Shear (VWS), (c) Flow Deformation (DEF) at 200-250 hPa from 1981 to 2010 based on ERA5 reanalysis. Zonal wind speed climatology at 250 hPa level is shown by the black contours (every 10 m s^{-1}, for wind speeds $\geq$ 20 m s^{-1}). Units are in %.

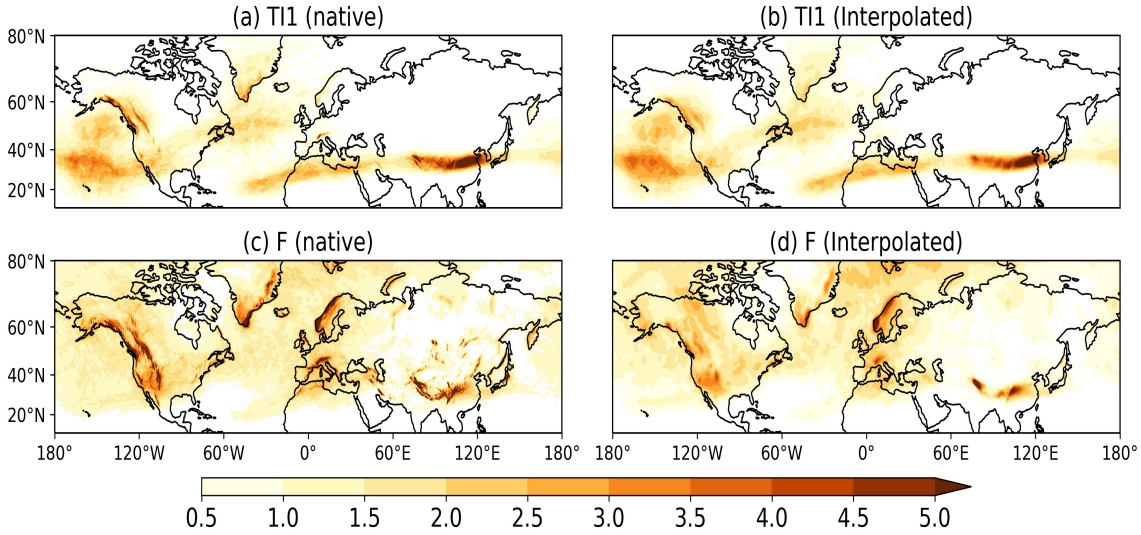

Figure 2. Winter (DJF) climatology of MOG-CAT frequency (≥ 0.5) at 200-250 hPa from 1981 to 2010 based on ERA5 native grid (left) and interpolated grid (right) for (a-b) Turbulence index 1 (TI1), (c-d) frontogenesis function. Units are in %.

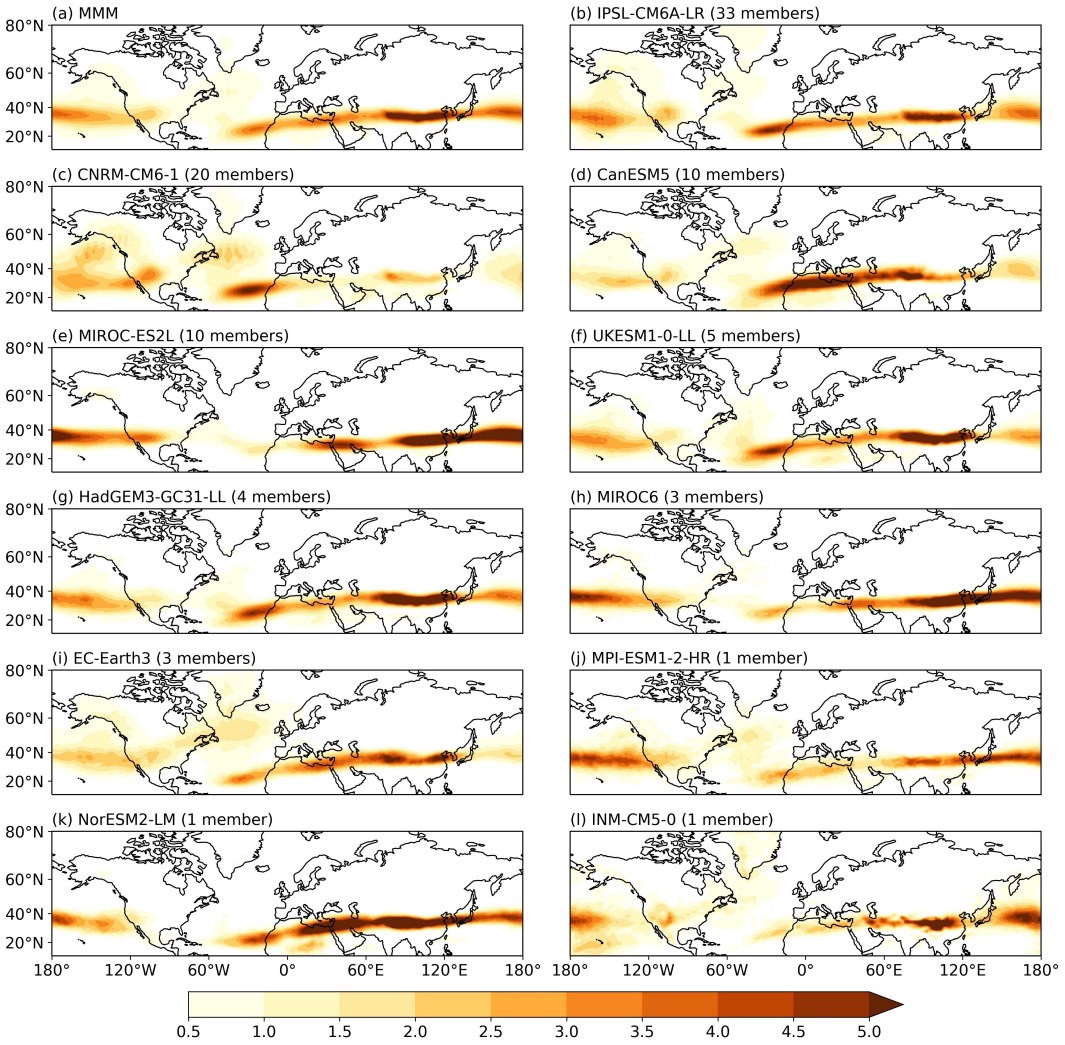

Figure 3. Winter (DJF) climatology of MOG-CAT frequency (≥ 0.5) of the Turbulence Index 1 at 200-250 hPa between 1981-2010 from (a) Multi-Model ensemble Mean (MMM) and (b-l) different CMIP6 climate models. Units are in %.

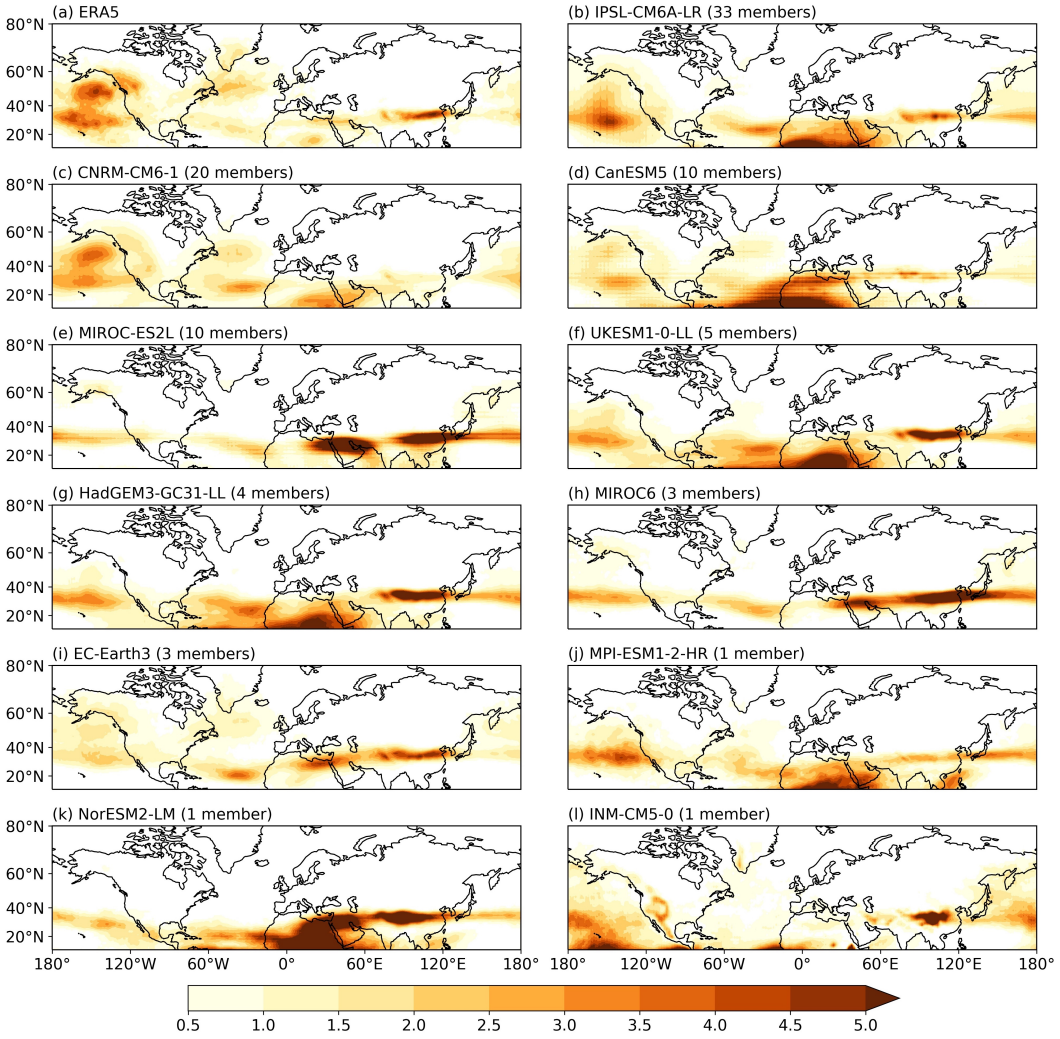

Figure 4. Winter (DJF) climatology of MOG-CAT frequency ($\geq 0.5\%$) of vertical wind shear diagnostic at 200-250 hPa between 1981-2010 from (a) ERA5 reanalysis and (b-l) different CMIP6 climate models. Units are in %.

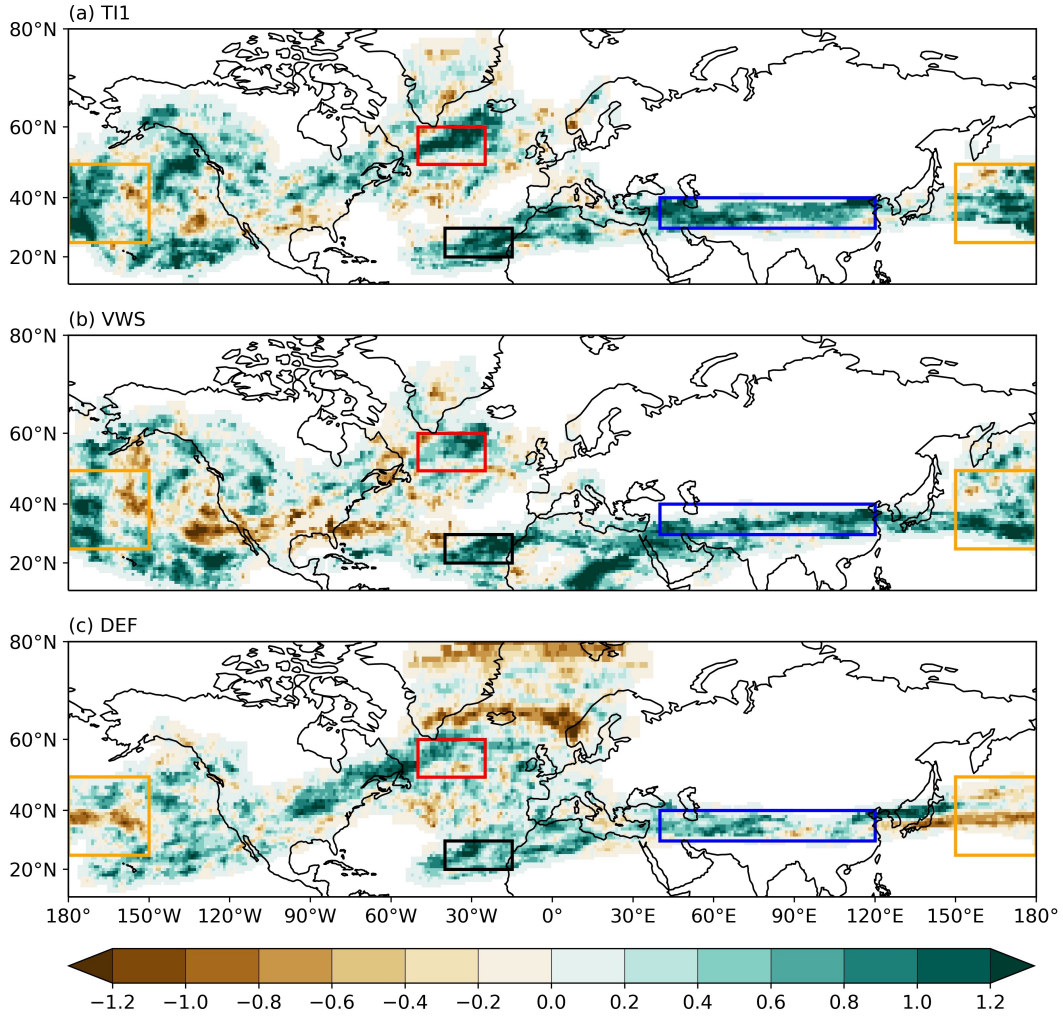

Figure 5. Ratio between the value of the trend and the interannual variability for MOG-CAT frequency estimated over the period 1980-2021 from ERA5 for (a) Turbulence Index 1 (TI1), (b) Vertical Wind Shear (VWS), (c) Flow Deformation (DEF) at 200-250 hPa for the winter season. Red, black, blue and orange boxes indicate Northern North Atlantic (NA) (50-25°W, 50-60°N), Southern NA (40-15°W, 20-30°N), Middle-East and East-Asia (40-120°E, 30-40°N), North Pacific (150°E-150°W, 25-50°N) regions respectively.

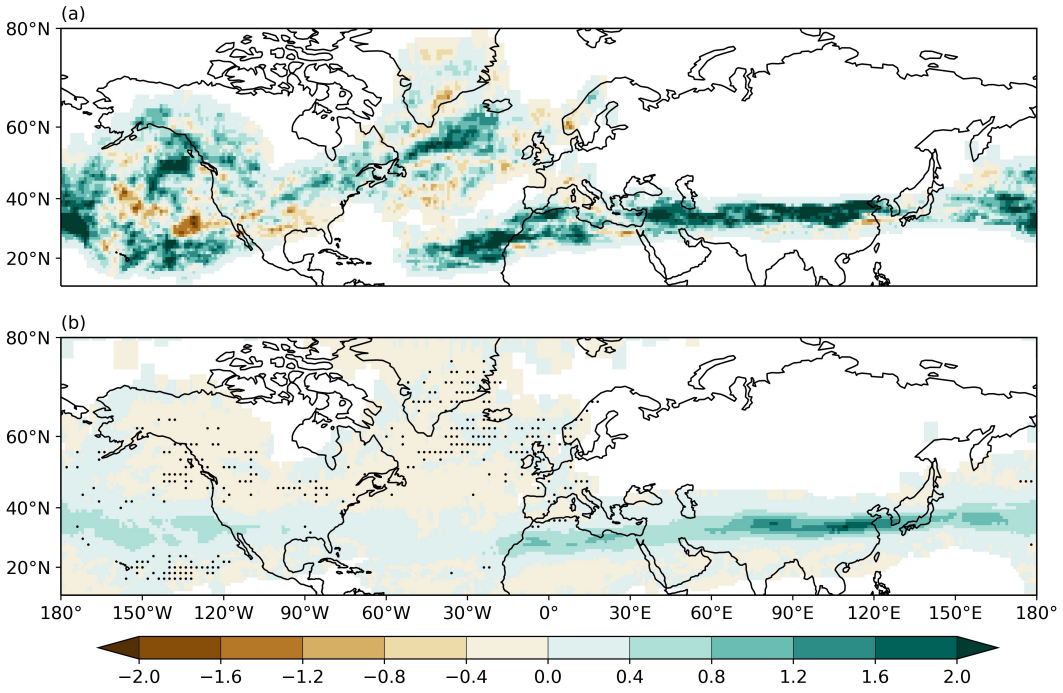

Figure 6. Winter (DJF) MOG-CAT frequency trends for Turbulence index 1 at 200-250 hPa over the period 1980-2021 from (a) ERA5 reanalysis, (b) The multi-model ensemble mean. The black dots in (b) indicate where the observed MOG-CAT trend in ERA5 is outside the range of the forced trends in the multi-model ensemble members.

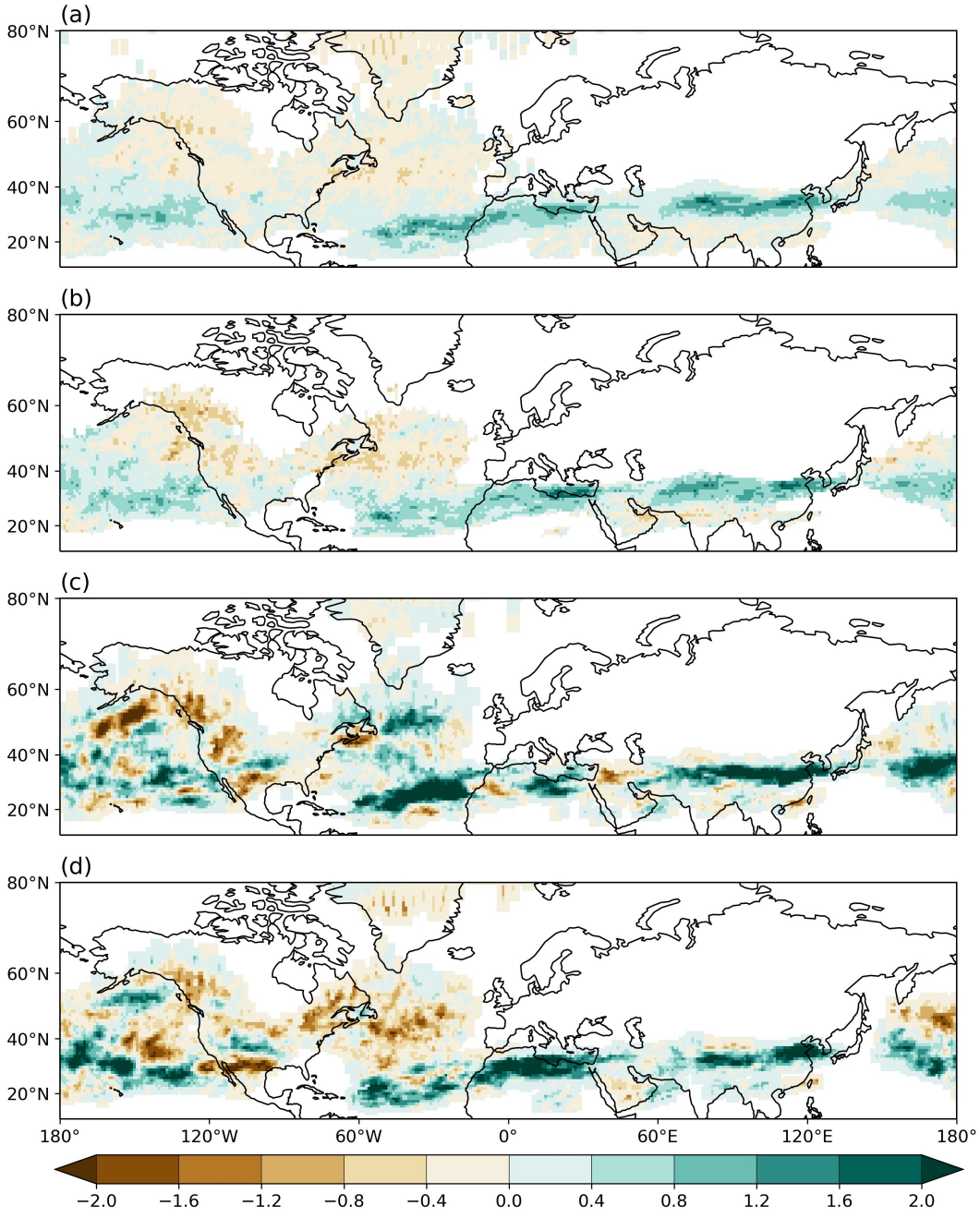

Figure 7. Winter (DJF) MOG-CAT frequency trends for Turbulence index 1 at 200-250 hPa over the period 1980-2021 from (a) The CNRM-CM6-1 model ensemble mean, (c) member 15, (d) member 16. (b) Signal-to-noise ratio from the 20 CNRM-CM6-1 ensemble members.

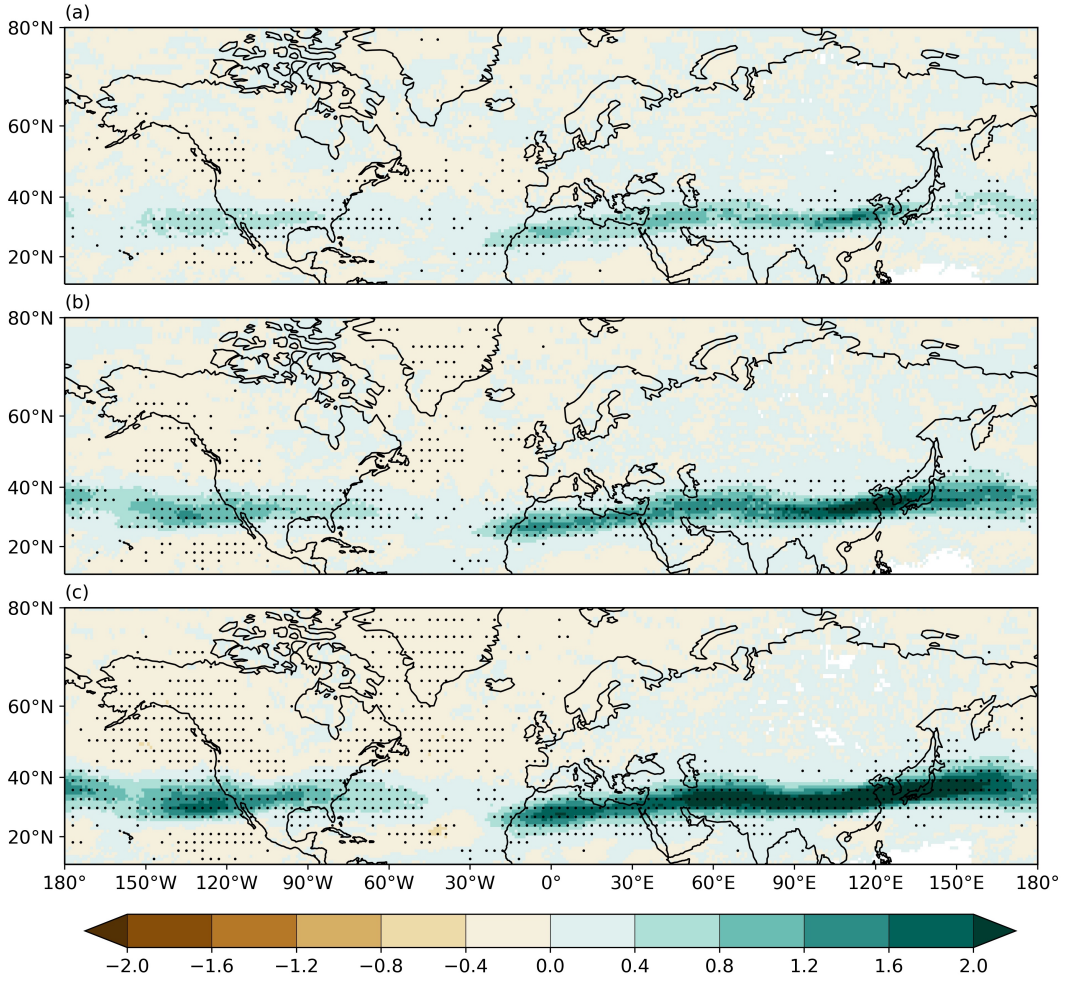

Figure 8. Projected changes in MOG-CAT frequency for Turbulence Index 1 at different global warming levels explained in the text: (a) ΔT=1°C, (b) ΔT=2°C and (c) ΔT=3°C. Changes are estimated from the multi-model ensemble mean. The black dots indicate those grid points where more than 80% of models agree on the sign of the change. Units are in %.

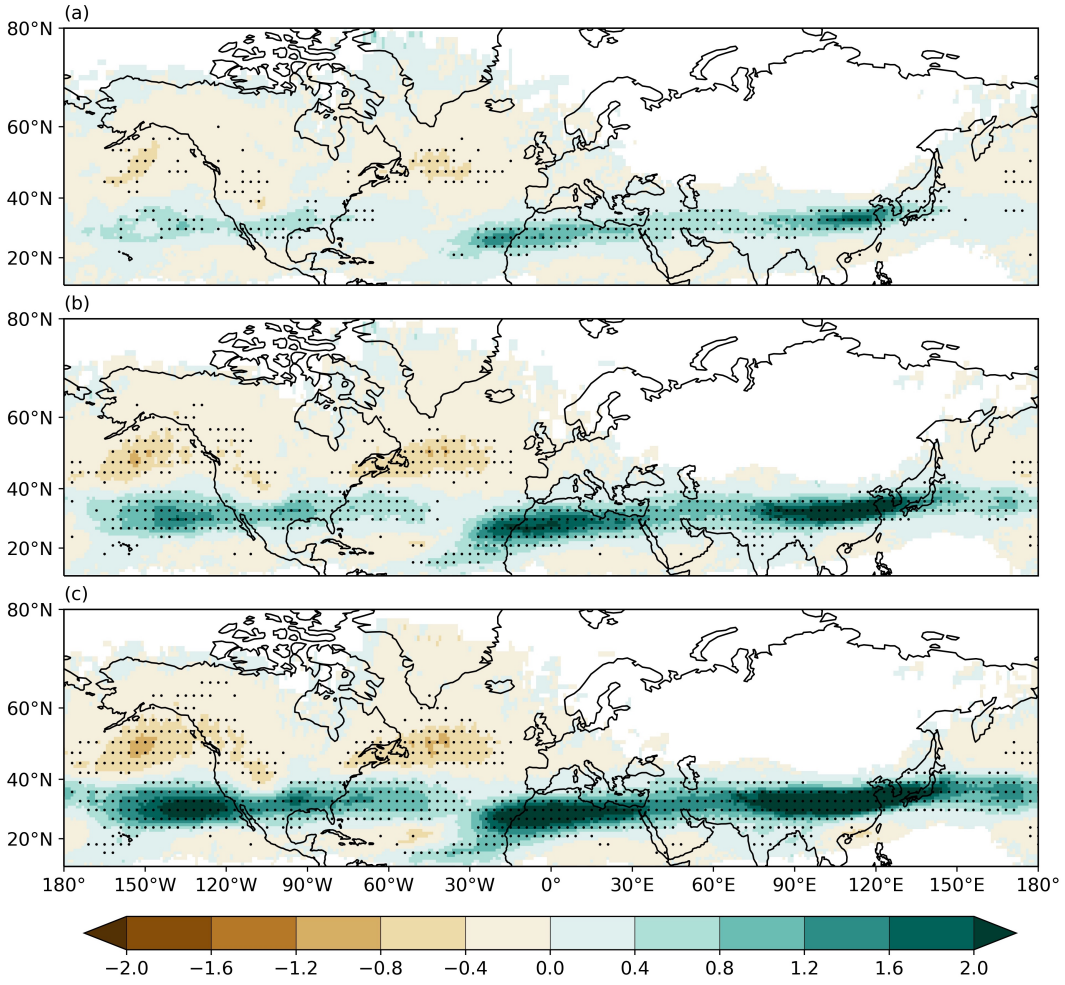

Figure 9. Projected changes in MOG-CAT frequency for Turbulence Index 1 at different global warming levels explained in the text: (a) ΔT=1°C, (b) ΔT=2°C and (c) ΔT=3°C. Changes are estimated from the CNRM-CM6-1 model ensemble mean. The black dots indicate those grid points where more than 80% of members agree on the sign of the change. Units are in %.

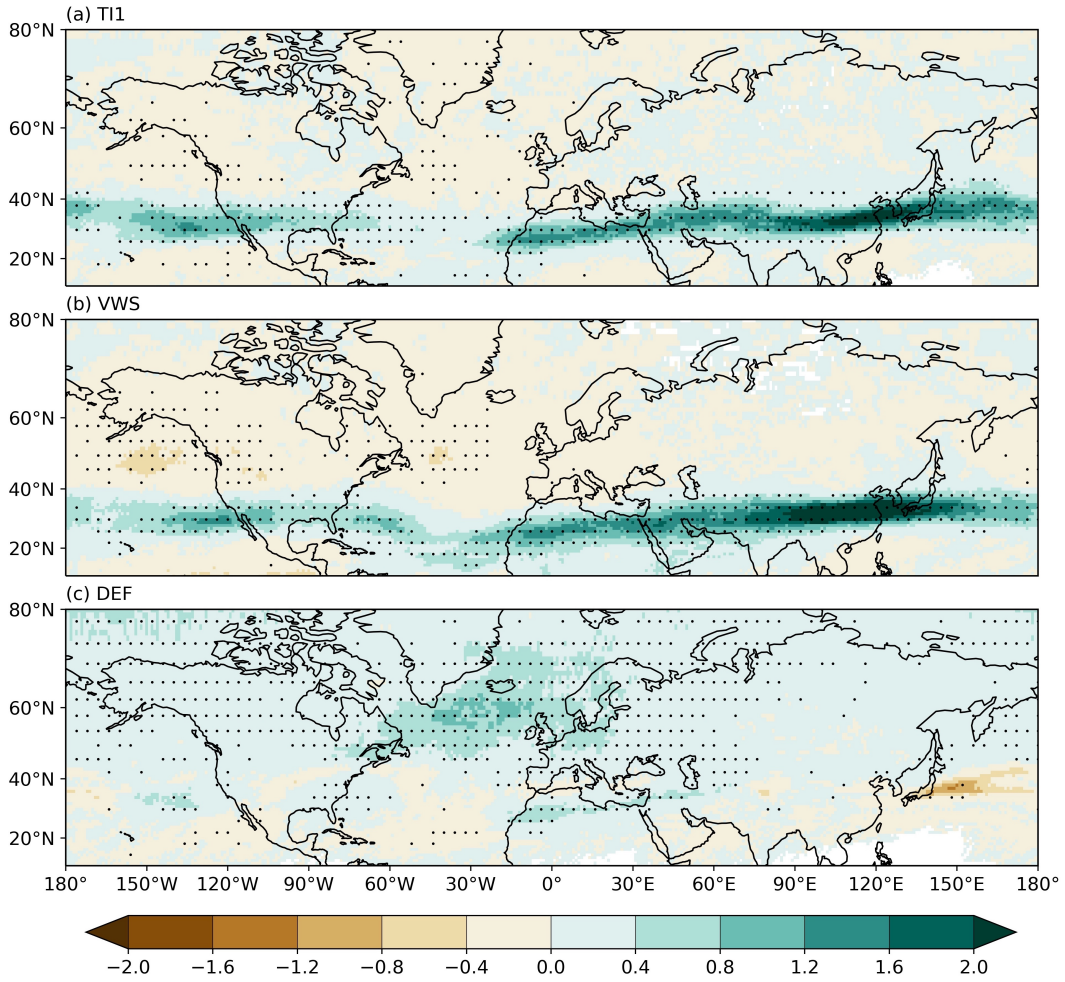

Figure 10. Projected changes in MOG-CAT frequency at ΔT=2°C for (a) Turbulence Index 1 (TI1), (b) Vertical Wind Shear (VWS), (c) Flow Deformation (DEF). Changes are estimated from the multi-model ensemble mean. The black dots indicate those grid points where more than 80% of models agree on the sign of the change. Units are in %.

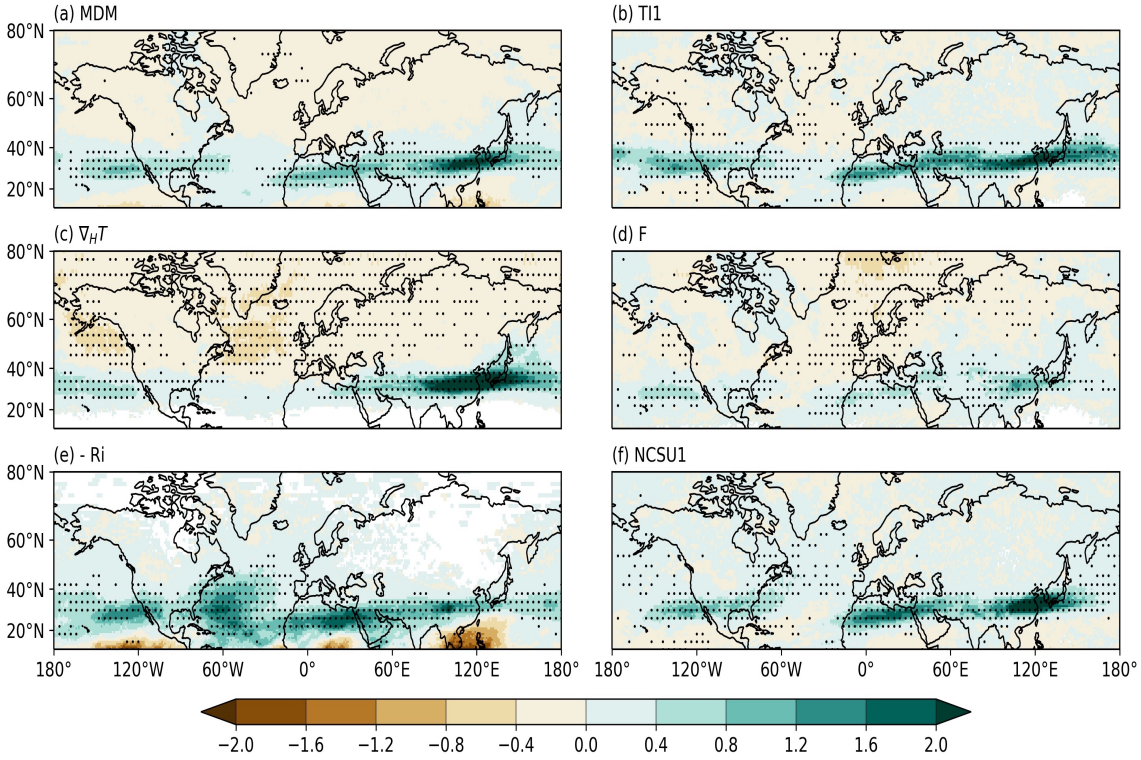

Figure 11. Projected changes in MOG-CAT frequency at ΔT=2°C for (a) the multi-diagnostic mean (MDM), (b) Turbulence Index 1 (TI1), (c) horizontal temperature gradient ($\nabla_H T$), (d) Frontogenesis function (F), (e) negative Richardson number (- Ri), and (f) North Carolina State University index 1 (NCSU1). Changes are estimated from the multi-model ensemble mean. The black dots in (a) indicate those grid points where all CAT indices agree on the sign of the change, while in (b-f) they indicates where more than 80% of models agree on the sign of the change. Units are in %.

Past and Future Trends in Clear-Air Turbulence over the Northern Hemisphere

Mohamed Foudad[1], Emilia Sanchez-Gomez[1], Thomas Jaravel[1], Mélanie C. Rochoux[1], and Laurent Terray[1]

[1]CECI, Université de Toulouse, CERFACS/CNRS, Toulouse, France

Key Points:

- Atmospheric reanalyses show increases in the frequency of Clear-Air Turbulence (CAT) in recent decades over several regions
- The increases over some regions could be attributed to global warming. In the North Atlantic, the increases are due to natural variability
- CAT frequency is projected to increase in the future over East Asia, Middle East, North Africa, North Pacific and North America

Corresponding author: M. Foudad, foudad@cerfacs.fr

Abstract

Clear-Air Turbulence (CAT) is associated with wind shear in the vicinity of jet streams in upper atmospheric levels. This turbulence occurs in cloudless regions and causes most weather-related aircraft accidents. Recent studies have shown that in response to climate change, CAT could significantly increase over certain regions as a consequence of strengthening of jet streams. In this study we use several atmospheric reanalyses and coupled model experiments database to evaluate CAT recent and future changes in the Northern Hemisphere. Several CAT diagnostics are computed to assess the sensitivity of results to different turbulence representations. A significant positive trend in CAT frequency is found in the reanalyses in different regions in the Northern Hemisphere over the period 1980-2021. The signal-to-noise analysis shows that over North Africa, East Asia and Middle East the increase of CAT occurrence in the last decades is likely attributed to global warming. In contrast, over the North Atlantic and North Pacific the internal climate variability is too strong to detect a response to anthropogenic forcing in the observed trends. Future climate projections show that over several regions in the Northern Hemisphere, CAT is projected to increase with a high model agreement and independently of the CAT diagnostic used. The largest increase in CAT is projected to occur over East Asia. In the North Atlantic, large uncertainty remains due to lack of model agreement and differences among the various CAT diagnostics.

Plain Language Summary

Aircrafts in flight can be subject to Clear-Air Turbulence (CAT), which is defined as all turbulence that occurs in the atmosphere away from a visible convective activity, and which is particularly difficult to detect by pilots and using on-board radar. CAT can injure passengers and flight attendants, cause structural damage to planes and induce considerable economic loss. In this study we use several atmospheric reanalyses and coupled model experiments database to evaluate CAT recent and future changes in the Northern Hemisphere. We also compute several CAT diagnostics to evaluate the sensitivity of results to different turbulence representations. Our results show that over several regions in the Northern Hemisphere, in particular East Asia, positive CAT trends are found as a consequence of anthropogenic forcing, indicating that the response of CAT to global warming can be already detectable in the recent decades. Positive trends in CAT frequency are projected to increase for different global warming levels over these regions at aircraft cruising altitudes. Nevertheless, over the North Atlantic region there are still many uncertainties in the response of climate models and also in CAT diagnostics used. The changes in CAT described in this study could have important consequences for aviation safety.

1 Introduction

Atmospheric turbulence is responsible for 71% of all weather-related aircraft accidents (Gultepe et al., 2019). Turbulence events can injure passengers and flight attendants, and in some rare cases, fatalities have occurred (Ellrod et al., 2015). It is also the cause of many people's fear of air travel (Sharman et al., 2012). The number of turbulence-related injuries is probably underestimated, because as pointed by Sharman et al. (2006), not all injuries are reported. Besides, repeated turbulence encounters over the lifetime of the aircraft may lead to material fatigue and can cause structural damage to aircraft (Ellrod et al., 2015). Thus, turbulence encounters are a safety issue, but they also cost to the airlines millions of dollars, and may cause flight delays and increasing fuel consumption and emissions (Sharman & Lane, 2016; P. D. Williams, 2016).

The main sources of atmospheric turbulence are: convective turbulence, mountain wave turbulence, and clear-air turbulence (CAT). In some cases, more specifically over high mountain chains (e.g., Himalayas, Rocky Mountains, Alps), distinguishing CAT from

mountain wave turbulence is unclear. Turbulence in clouds and thunderstorms can easily be detected visually by pilots and using on-board radar. In contrast, CAT is invisible and cannot be seen by pilots or radars, and is particularly difficult to detect and avoid. Because of this, CAT is the major cause of aviation turbulence and has a significant impact on aviation safety (Sharman & Lane, 2016).

CAT is defined as all turbulence that occurs in the atmosphere at altitudes of 5.6 km (∼500 hPa) or higher away from a visible convective activity. This includes turbulence found in cirrus clouds not in or adjacent to visible convective activity (Ellrod et al., 2015; Sharman & Lane, 2016). CAT often occurs near the tropopause level, where jet streams blow from west to east in the midlatitudes of both hemispheres (Dutton & Panofsky, 1970; Ellrod et al., 2015). The principal mechanism of CAT generation is the Kelvin-Helmholtz instability (Dutton & Panofsky, 1970; Ellrod & Knapp, 1992; Sharman & Lane, 2016). Kelvin-Helmholtz instability occurs when vertical wind shear is too strong to overcome the dampening influence of static stability. Vertical wind shear is, therefore, the most important ingredient for generating CAT. The environmental conditions favourable for a large vertical wind shear are found near jet streams and upper-level atmospheric fronts. About two-thirds of CAT occurrences are found near the jet streams (Ellrod et al., 2015). Breaking gravity waves induced by high mountains and by convection contribute also to CAT production (Ellrod et al., 2015; Storer et al., 2019).

Given its negative consequences for aviation safety, operational weather prediction centres provide daily CAT forecasts for airlines and air-navigation service providers. The spatial resolution of current numerical weather prediction models is too coarse to resolve explicitly turbulence (Ellrod & Knapp, 1992; Jaeger & Sprenger, 2007; Sharman & Lane, 2016; Sharman et al., 2006). However, turbulence in the atmosphere that affects aircraft is created by large-scale forcing mechanisms, which can be explicitly resolved by the numerical weather prediction models under the assumption that energy cascades down from larger scales into smaller eddies (Dutton & Panofsky, 1970; Sharman et al., 2006). Therefore, many CAT indices have been developed to diagnose regions where turbulence-generating mechanisms may likely occur, such as regions in which strong vertical and horizontal wind shear, horizontal deformation, and frontogenesis are present.

CAT variations in frequency and intensity are tightly related to jet stream changes at different timescales. In the context of global warming, previous studies have suggested that in response to greenhouse gas (GHGs) forcing, the midlatitude meridional temperature gradient in the upper troposphere may strengthen because of the polar lower-stratospheric cooling and tropical upper-tropospheric warming (J. H. Lee et al., 2023; S. H. Lee et al., 2019; Shaw et al., 2016). In consequence, jet streams and hence vertical wind shears could also increase, potentially inducing changes in CAT (P. D. Williams & Joshi, 2013). Indeed, recent studies have shown that vertical wind shear has increased during the last decades in response to the enhanced upper-level meridional temperature gradient (J. H. Lee et al., 2023; S. H. Lee et al., 2019; Lv et al., 2021). Jaeger and Sprenger (2007) found an increase of 40–90% in CAT frequency over different regions of the Northern Hemisphere by using ERA40 reanalysis (Uppala et al., 2005) in the period 1958-2001. More recently J. H. Lee et al. (2023) used CAT indices applied to ERA5 reanalysis and reported that the most significant increasing trend in CAT frequency during the last decades is located over East Asia. By comparing pre-industrial and doubled-CO2 climate simulations, P. D. Williams (2017) shows that CAT frequency may increase significantly in the future over the North Atlantic region. Storer et al. (2017) used climate future projections from CMIP5 (Coupled Model Intercomparison Project Phase 5) to assess CAT changes at global scale. They show an increase in CAT frequency across the globe, especially in the midlatitudes.

All these studies applied CAT indices to fields issued from atmospheric reanalyses and climate model experiments. Nevertheless, only one reanalysis or a single coupled model is used to evaluate recent and future CAT changes, which represents a limitation to assess

the climate uncertainty. Indeed, the main sources of uncertainties in climate change arise from i) the intrinsic climate variability, also called the internal climate variability; ii) the climate model formulation; and iii) the scenario of emissions (Hawkins & Sutton, 2011). In this study, we take into account the first two climate-related uncertainties while evaluating the past and future changes in CAT over the Northern Hemisphere. In addition, diagnostics used to characterize CAT may be also a source of uncertainty. We use here several atmospheric reanalyses and coupled model experiments from CMIP6, and a large ensemble member of 20 simulations performed with CNRM-CM6-1 model, in order to study the roles of the internal climate variability and the model uncertainty in CAT trends. We also compute several CAT diagnostics to analyse the sensitivity of our results to different turbulence representations. Note that we focus on Moderate-Or-Greater (MOG) CAT, which is known to have the greatest implications for in-flight safety (P. D. Williams & Joshi, 2013; Sharman et al., 2006). The datasets, numerical experiments and methodology are described in Sections 2 and 3, respectively. Results regarding the past and future CAT trends are presented and discussed in Section 4. Finally, in Section 5, the conclusions and prospects for future work are provided.

2 Data

To compute CAT indices, we use daily averages of wind, geopotential height and temperature fields from atmospheric reanalysis and climate model experiments. Three state-of-the-art atmospheric reanalyses in the period 1980 to 2021 are considered: (1) the ECMWF Reanalysis version 5 (ERA5) (Hersbach et al., 2020), whose spatial resolution is $0.25° \times 0.25°$; (2) the Japanese 55-year Reanalysis (JRA55) (Kobayashi et al., 2015) provided on a $1.25° \times 1.25°$ grid; and (3) the Modern-Era Retrospective analysis for Research and Applications, Version 2 (MERRA-2) (Gelaro et al., 2017) at $0.5° \times 0.625°$ spatial resolution.

Climate simulations performed with 11 different models from CMIP6 database (Eyring et al., 2016) are used. All these experiments are detailed in (Table 1). We consider only the models providing the daily mean outputs for atmospheric fields necessary to compute CAT indices (see Section 3). Two CMIP6 experiments are used: 1) the historical experiment, consisting in a climate reconstruction from the 1850-2014 period; and 2) the future projections performed under the scenario ssp5-8.5 from the Tier 1 of the Scenario Model Intercomparison Project (ScenarioMIP) (O'Neill et al., 2016). The ssp5-8.5 scenario induces the largest radiative forcing, i.e. the global warming, on the earth surface by the end of the twenty-first century. All the model data are used for the period 1970-2100.

For each experiment in 1) and 2), all the available ensemble members from the 11 coupled models are used. As the number of members is different from one model to another, we compute first the ensemble mean for a given model before computing the multi-model mean (MMM), assuring the same weighting in the MMM. In addition, a large ensemble member of 20 historical and SSP5-8.5 simulations was performed with CNRM-CM6-1 model to better estimate the signal-to-noise ratio in past and future CAT changes. All data from reanalyses and climate models were interpolated on a common $1° \times 1°$ grid before computing CAT diagnostics. A conservative remapping method was used for fields with a spatial resolution lower than 1°, whereas bilinear interpolation was applied for the rest.

3 Methods

3.1 Choice of CAT diagnostics

We focus on CAT produced by vertical wind shear and frontogenesis in upper tropospheric levels, where the core of the jet stream is located. Then, the Turbulence

Index 1 (hereinafter TI1) defined by Ellrod and Knapp (1992) and its two components, Vertical Wind Shear (VWS) and Flow deformation (DEF), are used here as CAT diagnostics. We made this choice as TI1 has shown significant skill to predict CAT encounters (Gill, 2014; Sharman et al., 2006). In particular, the probability of detection indicates that more than three-fourths of all CAT events are correctly detected by TI1 compared to pilots' reports (Ellrod & Knapp, 1992). Note that TI1 is widely used in many forecast weather centres (e.g. Météo-France, KNMI). The two World Area Forecast Centres (WAFC; London and Washington) also use TI1 as a single diagnostic to provide a global turbulence forecast on a $1.25° \times 1.25°$ grid (Gill, 2014; Kim et al., 2018; Storer et al., 2020), and TI1 is currently implemented in the graphical turbulence guidance algorithm (Sharman et al., 2006).

Following Ellrod and Knapp (1992), TI1 index is defined as the product of VWS and DEF:

$$TI1 = VWS \times DEF. \tag{1}$$

VWS is the wind field difference in the atmospheric layer:

$$VWS = \left((\frac{\partial u}{\partial z})^2 + (\frac{\partial v}{\partial z})^2 \right)^{\frac{1}{2}}, \tag{2}$$

where u is the horizontal wind velocity in the east–west direction, and v is the horizontal wind velocity in the north–south direction. The altitude z corresponding to the pressure level at each grid point is calculated by using the geopotential height. In addition, DEF combines Shearing Deformation (D_{SH}) and Stretching Deformation (D_{ST}):

$$DEF = \left(D_{SH}^2 + D_{ST}^2 \right)^{\frac{1}{2}} = \left((\frac{\partial v}{\partial x} + \frac{\partial u}{\partial y})^2 + (\frac{\partial u}{\partial x} - \frac{\partial v}{\partial y})^2 \right)^{\frac{1}{2}}. \tag{3}$$

DEF is computed at the top (200 hPa) and at the bottom (250 hPa) of the atmospheric layer. Then the resulting mean is taken as the total flow deformation in the layer (same method as in Overeem (2002)).

We select the atmospheric layer located between 200 and 250 hPa, which contains typical cruising altitudes of 10-12 km approximately. The winter season, defined here as December-January-February (DJF), is considered because this is the season where the frequency of CAT is higher in the Northern Hemisphere (Jaeger & Sprenger, 2007; J. H. Lee et al., 2023).

In order to assess the robustness of the results to the choice of CAT diagnostics, other CAT indices are used (see Section 4.4). These indices are: the negative Richardson number (- Ri), frontogenesis function, horizontal temperature gradient and the North Carolina State University index 1 (NCSU1). These indices were calculated at the same levels as those mentioned above.

3.2 Definition of the MOG-CAT category

To characterize MOG-CAT category, we followed the approach described in previous studies (J. H. Lee et al., 2023; Storer et al., 2017; P. D. Williams, 2017). This consists of defining a threshold value for a large commercial aircraft by calculating a percentile range from the probability density function of the CAT diagnostic. However, in the literature, there is no consensus on the choice of this threshold value. P. D. Williams (2017) and Storer et al. (2017) applied the 99.6th percentile as MOG-CAT threshold. This means that in the high atmosphere the probability of MOG-CAT occurrence is set to 0.4%. J. H. Lee et al. (2023) considered 5% as the probability of MOG-CAT occurrence (95th percentile), while based on pilots' reports, Sharman et al. (2006) found that the probability of upper-levels MOG-CAT is at most 1%.

In this study, we chose to apply the threshold value of 1% for MOG-CAT occurrence. This choice is also motivated by the fact that 1% also offers a larger sample size for a robust statistical treatment. Accordingly, the threshold of MOG-CAT is defined for each dataset by computing the 99th percentile from the probability density function of winter daily values over the reference period 1981-2010. Only midlatitude areas are considered, defined here as the 20-60°N latitudinal band (J. H. Lee et al., 2023).

It is worth mentioning that the spatial distribution of CAT frequency and its trends are weakly sensitive to the threshold used (not shown). We define MOG-CAT frequency at each grid point as the percentage of the values exceeding the threshold value. Note that the value of the threshold is very dependent on the horizontal resolution of the data used: the finer the resolution, the higher the threshold value. This is the reason why all the variables from the reanalyses and climate models were interpolated on a common grid before computing CAT diagnostics (see Section 2).

4 Results

4.1 MOG-CAT climatology in reanalysis and CMIP6 climate models

High frequencies of MOG-CAT occurrence are found over different regions in the Northern Hemisphere (Figure 1a): the North Atlantic, North Pacific, East-Asia and North Africa. This is consistent with previous studies, which have computed MOG-CAT climatology from other reanalysis and over different periods (Jaeger & Sprenger, 2007; J. H. Lee et al., 2023). In general, MOG-CAT occurs in the vicinity of jet-streams and the highest frequencies are located on the northern side of the jet. Very similar spatial patterns of MOG-CAT climatology are obtained from JRA55 and MERRA-2 reanalyses (not shown).

The maximum MOG-CAT frequency is located over East-Asia and can reach more than 7.0%. This is mainly due to strong VWS (Figure 1b), where the subtropical jet reaches its maximum speed. This is also due to the presence of the Himalayan mountain range that could enhance VWS. Other areas of large MOG-CAT occurrence are observed at the subtropical jet entrance, which is located over western North Africa. Here, the highest frequencies in MOG-CAT are induced by large DEF due to the presence of the Azores high (Figure 1c). It has been shown that regions of sharply curved anticyclonic flows most frequently produce CAT (Ellrod et al., 2015; Jaeger & Sprenger, 2007). Over North Pacific and northern North Atlantic areas, both VWS and DEF contribute to MOG-CAT generation (Figure 1a-c). MOG-CAT frequency peaks over high mountain chains (Himalayas, Rocky Mountains and Alps). Whereas the regridding of ERA5 onto a coarser grid does not significantly affect the spatial structure of TI1 index, the MOG-CAT characteristics over the mountainous areas are greatly affected by the interpolation for the frontogenesis function CAT diagnostic (Figure 2). This is probably due to the high resolution, which allows to better resolve the mesoscale mountain waves. However, there is no dependence on spatial resolution for MOG-CAT produced by vertical wind shear within jet-streams and upper-level fronts (Figure 2).

MOG-CAT climatology is well represented in CMIP6 models with respect to ERA5 which is considered as the reference here (Figure 3). The spatial structure of MOG-CAT occurring in the vicinity of the subtropical jet is in general well simulated in all models, although some of these models overestimate MOG-CAT frequency over East-Asia and North Pacific (MIROC-ES2L, UKESM1-0-LL) and others underestimate it (CNRM-CM6-1, CanESM5, MPI-ESM1-2-HR). Over the North Atlantic, most of the models underestimate MOG-CAT frequency except CNRM-CM6-1 and EC-Earth3, which represent better the spatial distribution of MOG-CAT. In general, over the North Atlantic, models simulate higher MOG-CAT frequency at lower latitudes, over the subtropical jet entrance. This is partly due to the fact that CMIP6 models feature a stronger VWS over the subtropical jet than over the polar jet with respect to ERA5

(Figure 4). Focusing on the MMM, MOG-CAT frequencies over East-Asia, North Africa and North Pacific are close to ERA5 (Figure 3). However, over the North Atlantic area, MMM MOG-CAT frequency is approximately twice weaker than in ERA5, pointing out that CMIP6 models display some deficiencies in simulating CAT extremes in this area.

4.2 MOG-CAT past trends

We define a common period, 1980-2021, to investigate past trends in MOG-CAT frequency. For this purpose, we compute at each grid point the trend (signal) of the interannual time series of winter MOG-CAT frequency by using a linear least-squares regression method. Then, the trend value is normalised by the interannual standard deviation (noise) of the time series. We proceed in this way to assess if the trend is larger than the interannual variability of MOG-CAT in winter. Note that to generate robust statistics, only the grid points showing a sufficient number of MOG-CAT episodes during the period of study were taken into account in the trend estimation. We selected the grids points with more than 50% values different from zero in the time-series, i.e. the grid points with more than 21 winters of non-zero MOG-CAT values. We proceed in the same way to assess VWS and DEF trends.

Figure 5a shows that for ERA5, the largest positive values of the signal-to-noise ratio are observed in several regions: East Asia, Middle East, North Pacific and North Atlantic. The increase in MOG-CAT frequency over the last decades in these different regions is associated with a large increase in VWS (Figure 5b) over the jet streams. VWS near jet-streams is highly correlated with the meridional temperature gradient according to the thermal wind balance. This suggests that the increase in VWS could be related to the positive trends in the meridional temperature gradient in the upper levels, which are likely due to the tropical upper-tropospheric warming and the polar lower-stratospheric cooling during the recent decades (J. H. Lee et al., 2023). Over the North Atlantic, the positive trends in MOG-CAT are driven by both VWS and DEF (Figure 5b and 5c).

We assess MOG-CAT trends obtained with other reanalyses over the four regions indicated with the boxes in Figure 5. In the North Atlantic, we consider two domains: (i) North Atlantic polar-jet exit; and (ii) Southern North Atlantic subtropical-jet entrance. This splitting allows to separate CAT produced by the polar jet from that produced by the subtropical jet. The polar jet stream is often described as eddy-driven and is distinct from the subtropical jet stream, which is primarily caused by poleward transport of angular momentum in the Hadley cell (S. H. Lee et al., 2019). The other two domains are: (iii) North Pacific, where the two polar and subtropical jets merge; and (iv) Middle-East and East-Asia, where CAT is mainly produced by the subtropical-jet and strengthened by the Himalayas. These regions have been selected because large positive trends are observed in recent decades (Figure 5). Besides, these regions are characterised by a high density of air traffic linking Europe, North America, East Asia and Middle-East.

For each region, the winter annual MOG-CAT frequency is defined by computing the percentage of the values that exceeds MOG-CAT threshold relative to the total number of values (number of grid points $\times$ number of winter days of each year). Then, the percentages of change shown in (Table 2) are obtained using the total change for the whole period (slope of the trend line $\times$ 42 years) compared to the frequency in 1980 of the fitted linear trend lines.

ERA5, JRA55 and MERRA-2 are in good agreement with the increase of MOG-CAT over the four regions (Table 2). A mean percentage of change of 61.8% was obtained over northern North Atlantic for MOG-CAT and 155.9% over southern North Atlantic. Over the North Pacific MOG-CAT increases by 61.1%, and over East Asia and Middle East by 106% on average. Note that the values of the increases are much higher with JRA55 compared to ERA5 and MERRA-2 over southern North Atlantic, East Asia and Middle

East. The trends are generally robust and statistically significant at 1% level (p-value $<$ 0.01), except over the northern North Atlantic. The largest increases of MOG-CAT are found over Northwestern Africa, East Asia and Middle East, where MOG-CAT frequency has more than doubled between 1980 and 2021, mainly due to a sharp increase in VWS.

Next step is to investigate the possible causes of these MOG-CAT increases. To analyse the respective role of internal versus externally forced variability, we use the historical experiments performed by CMIP6 models (Table 1). The multi-model multi-member ensemble allows to isolate the forced climate response from the internal climate variability. The externally forced component of the simulated MOG-CAT trends can be obtained by averaging the trends from all the members together (Deser et al., 2014, 2016).

Figure 6 compares the observed MOG-CAT trends in ERA5 with the forced MOG-CAT trends in CMIP6 models. Like the observed trend pattern, the forced response shows some evidence for the increase of MOG-CAT frequency over East Asia, Middle East and North Africa. This indicates that the MOG-CAT response to global warming is strong enough to be detected over these regions, pointing out the potential influence of human-induced climate factors on these trends. Over the North Atlantic and the North Pacific, there is no agreement between the observed MOG-CAT trend and the forced response, suggesting that the internal climate variability is still very large with respect to the GHGs effect in these regions. Overall, the values of the observed MOG-CAT trends lie within the range of simulated predictions, except over the northern North Atlantic and North America (Figure 6).

In complement, we also used only the 20 members of the CNRM-CM6.1 model to isolate the effects of anthropogenic climate change from those of internal variability on MOG-CAT trends. A forced response similar in pattern to that of the multi-model ensemble members was obtained (Figure 7a). In addition, here we provide a quantitative assessment using a simple signal-to-noise analysis. The signal is obtained by averaging across the 20 members of the CNRM-CM6.1 model, and the noise is the spread amongst all the members (Deser et al., 2014, 2016). High positive values of the signal-to-noise ratio are found over East Asia, Middle East and North Africa (Figure 7b), indicating that the changes in MOG-CAT frequency could be attributed to a response of the atmosphere to external forcings (i.e. GHG increases) over these regions. In contrast, over the North Atlantic and the North Pacific, the signal-to-noise ratio is very weak, suggesting that the amplitude of internal variability in recent decades is still very strong to make the global warming signals detectable. Over the North Atlantic, the individual ensemble members reveal a wide range of MOG-CAT trend responses to the same external forcing. For example, members 15 and 16 exhibit opposite sign (Figure 7c and 7d). Our findings are in agreement with the study by Tenenbaum et al. (2022), which used 20 years of aircraft observations of the New York to London flights over North Atlantic and which reported that the turbulence trends are not statistically significant. Our findings are also consistent with the study by J. H. Lee et al. (2023), in which the largest positive MOG-CAT trends were found in East Asia between 1979 and 2019.

4.3 MOG-CAT future changes

We investigate MOG-CAT changes in the future climate projections by considering different global warming levels (GWLs) rather than the time horizon. For this purpose, we apply the epoch approach, also called the time-shift method, used in the International Panel on Climate Change (IPCC) AR6 report (see section 4.6.1 in Masson-Delmotte et al. (2021)). As mentioned in the IPCC AR6, this method offers significant advantages compared to the widely-used time horizon approach, since it allows future projections to be combined independently from the emissions scenarios and the climate sensitivity in coupled models. Moreover, the use of GWLs to assess changes in extreme events is more meaningful for decision makers as actionable information is provided (IPCC AR6,

chapter 11). The method consists of setting different GWL levels (1°C, 2°C, 3°C, 4°C) with respect to the 1850–1900 period. Here we define the reference as GWL = 1°C , which in fact corresponds to the GWL currently observed (∼1.1°C). We consider three different future climates at GWLs = 2°C, 3°C, 4°C. We first proceed by computing 20-year moving averages of the global average surface temperature for each member of each model. Note that the year in which a GWL is exceeded is different across the different simulations. Then we examine when the required GWL is reached with respect to our reference GWL. Once the year in which the GWL was exceeded is obtained, a 20-year period centred on this year is computed. This 20-year period is used to be representative of the required GWL and composites for other variables can be obtained by using this period. Finally, for each member of each model, MOG-CAT frequency is calculated for the present GWL = 1°C and for each future GWL=2°C, 3°C, 4°C and the respective differences are computed. We note here ΔT the global mean temperature difference between each future GWL and the present GWL.

Large increases in MOG-CAT frequency are projected over most regions within the latitudinal band 20-40°N, located over East Asia, Middle East, North Africa, North Pacific and North America (Figure 8). Moreover, there is generally a high model agreement about this increase. These projected changes in MOG-CAT frequency are enhanced as the GWL increases. However, at higher latitudes the values of the projected changes obtained by the MMM are small with low model agreement, in particular over the North Atlantic. However, these uncertainties are much reduced for ΔT=2°C and 3°C, for which the MMM projects a reduction of the MOG-CAT in the future (Figure 8b and 8c).

We use the large ensemble of CNRM-CM6.1 model to investigate the role of the internal variability on the different GWL projections. This is measured as the agreement amongst the 20 members of the ensemble (Figure 9). The effects of internal variability on the MOG-CAT frequency are moderate for ΔT =1°C, but very weak for larger GWLs, since a high member agreement is obtained. As expected, the response of external forcing (GHGs) becomes dominant as GWL increases. CNRM-CM6.1 projections are similar to the MMM response shown in Figure 8, indicating the appropriateness of using large ensembles (Deser et al., 2014, 2012; Kay et al., 2015).

Figure 10 suggests that the projected changes in MOG-CAT frequency shown in Figure 8 are mostly caused by the increase in VWS within the subtropical jet (20-40°N latitudinal band). According to the thermal wind balance relation, the increase of VWS in the last four decades is highly correlated with the strengthening of the meridional temperature gradient (J. H. Lee et al., 2023). Our results would support that the meridional temperature gradient is likely projected to be reinforced in the future climate as a response to anthropogenic climate change, leading to stronger subtropical jet and an increase in VWS. Despite the increase in DEF over the North Atlantic, the combination with VWS shows a weak decrease in MOG-CAT (Figure 10).

It is worth noting that we find no impact of the model horizontal resolution on the results. Indeed, the ensemble of CMIP6 models used in this study includes two high-resolution models. We found no differences in the results on the original and interpolated grids (not shown). Further, by comparing ERA5 in the native grid (∼25 km) and interpolated grid (∼100 km), we found very similar results in MOG-CAT climatology and trends (Figure 2). This is consistent with the study by Smith et al. (2023): they used three different models with high and coarse resolutions for each one, and they found no dependence on model resolution for moderate CAT projections over the North Atlantic.

4.4 Extension to other CAT indices

An extension of the analysis to other CAT indices is carried out to assess the uncertainty associated with the different CAT diagnostics. We select an ensemble of 5 CAT diagnostics, whose predictive skill to characterize CAT has been demonstrated and

validated with observational data (P. D. Williams & Storer, 2022; Sharman et al., 2006). Besides TI1 index, the new diagnostics include: frontogenesis function, horizontal temperature gradient, - Ri, and NCSU1. They are described in detail by Sharman et al. (2006). These indices are currently implemented in the graphical turbulence guidance algorithm. Sharman et al. (2006) showed that these diagnostics perform best in forecasting upper-level turbulence phenomena. Using this subset therefore ensures that the results are as robust as possible. Note that our approach differs from previous studies, which use a large number of turbulence diagnostics (P. D. Williams, 2017; Storer et al., 2017; Smith et al., 2023); most of these diagnostics are important ingredients in CAT production but cannot be considered as CAT indices when used alone.

The spatial patterns of projected changes in MOG-CAT frequency for ΔT=2°C are similar among the CAT diagnostics (Figure 11). Large increases in MOG-CAT frequency are obtained over different regions in the latitudinal band 20-40°N (East Asia, Middle East, North Africa, North Pacific and North America). Note that the frontogenesis function presents weaker changes compared to the other indices but they are located in the same areas. Figure 11 shows that over East Asia, Middle East, North Africa, North Pacific and North America, the multi-diagnostic multi-model mean is quite in agreement on an increase in MOG-CAT frequency as a consequence of global warming. The largest increases in MOG-CAT frequency are projected to occur over East Asia.

Again, over the North Atlantic, the projected changes are weak and there is less agreement amongst the CAT diagnostics. The sign of the change is negative for three out of the five indices used (TI1, horizontal temperature gradient, frontogenesis function) and positive for - Ri and NCSU1, which takes into account Ri in its computation. Ri is defined as the ratio between the squared Brunt-Väisälä frequency N^2 (which is related to static instability) and the squared VWS. This indicates that projected increase in MOG-CAT frequency shown by Ri over the North Atlantic is mostly explained by the increases in the static instability rather than by VWS, which is projected to decrease over this area (Figure 11). Indeed, the use of Ri to characterize CAT could be misleading, since the static instability, although a turbulence measure, can also be related to convective turbulence which is visible. The climatology of Ri shows that the highest frequencies are located over the tropics, which are well known to be regions of convective turbulence (not shown). Another limitation of using Ri is that this index is more reliable when estimated from high-resolution data (Ellrod et al., 2015).

Our results suggest that the uncertainty in MOG-CAT projections over North Atlantic between CAT indices is related to the competition between changes in the wind shear and convective instability phenomena, both sources of turbulence. It is important to recall that wind shear instability is the most important ingredient in CAT generation (Dutton & Panofsky, 1970; Ellrod et al., 2015; Sharman & Lane, 2016). This uncertainty linked to CAT diagnostics implies that the CAT phenomenon is complex and that all the phenomena that generate it should be studied in order to understand future changes.

The disagreement in CAT projections amongst twenty diagnostics can also be found in Figure 2 of Storer et al. (2017) based on the HadGEM2-ES model. Over the North Atlantic, the TI1 index shows a weak decrease. In contrast, DEF increases considerably (up to 500%), which is consistent with our results (Figure 11). More recently, Smith et al. (2023) found that over the North Atlantic, twelve diagnostics projected a moderate CAT increase, while six projected a decrease. Furthermore, P. D. Williams and Storer (2022) showed a strong inter-diagnostic uncertainty in CAT climatology and trends with ERA-interim reanalysis and HadGEM2-ES model. Thus, while it is crucial to study CAT changes from a multi-diagnostic approach, averaging across all diagnostics may complicate interpretation of results since the diagnostics can represent very different physical phenomena.

5 Conclusions and Discussion

This study provides an assessment of past and future changes in MOG-CAT frequency over the Northern Hemisphere by using different atmospheric reanalyses and experiments performed with 11 CMIP6 climate models.

Consistently with previous studies (Jaeger & Sprenger, 2007; J. H. Lee et al., 2023), we find that highest frequencies of MOG-CAT occurrence in the current climate are located on the northern side of the jets over different regions: the North Atlantic, North Pacific, East-Asia and North Africa. The maxima of MOG-CAT frequency were found over East-Asia (approximately 7.5%), which are due to strong vertical wind shear (VWS) where subtropical jet reaches its speed maximum, and which are also due to the presence of the Himalayas that could enhance VWS. In addition, this study performs the first validation of CMIP6 models in terms of simulated MOG-CAT climatology with different CAT diagnostics. We conclude that these models are suitable tools to study MOG-CAT. Nevertheless, we show that over the North Atlantic region, most models underestimate MOG-CAT frequency, mainly due to the fact that CMIP6 models simulate weaker vertical wind shear within the polar jet with respect to ERA5 reanalysis (Figure 4).

Past changes in MOG-CAT frequency for the period 1980-2021 show increases in East Asia, Middle East, North Africa and North Pacific. The different atmospheric reanalyses are in good agreement and the trends are statistically significant at 1% level. Over the North Atlantic, the reanalyses show positive trends that are not statistically significant. We find that in recent decades, frequency of MOG-CAT has more than doubled over Northwestern Africa, Middle East, and Eastern Asia. This is mainly due to a large increase in VWS related to the subtropical jet strengthening, which is due in turn to the sharpening of the meridional temperature gradient caused by the warming over the tropics and the cooling over high latitudes in upper atmospheric levels. The importance of the internal climate variability with regards to the anthropogenic forcing is addressed by using CMIP6 models and a large ensemble performed with the CNRM-CM6.1 model. We find that over the North Pacific and the North Atlantic regions, the internal climate variability is large enough to mask the anthropogenic-induced signal. In addition, the increase in MOG-CAT frequency observed in East Asia and Middle East over the last four decades is outside the range of internal variability and could be potentially attributed to external forcing.

Multi-model climate projections indicate that the positive trend reported over North Africa, East Asia and Middle East will continue to increase in the future with the global warming level, and there is a high agreement amongst the climate models and the CAT diagnostics. In general, models project a MOG-CAT increase within the 20-40°N latitudinal band and a weak decrease northwards. The projected increases in MOG-CAT frequency over these regions intensify with the degree of global surface warming considered. Component analysis of the TI1 CAT index leads to the conclusion that increases in MOG-CAT frequency are mainly related to increases in VWS within the subtropical jet. Contrary to previous studies (P. D. Williams, 2017; Storer et al., 2017; Smith et al., 2023), our results show a slight decrease in MOG-CAT frequency over the North Atlantic. The disagreement over this region can be explained by the fact that there are large uncertainties associated with the CAT indices used. We suggest that this uncertainty may be linked to competition between vertical wind shear and convective instability, both sources of turbulence. However, it is important to recall that shear instability is the main source of clear-air turbulence, and that vertical wind shear is projected to decrease over the North Atlantic.

The projected increases in MOG-CAT frequency shown in this study could have a significant impact on aviation operations and safety, as well as on the design of future aircrafts. Future work is needed to extend the analysis to other atmospheric layers (e.g., 150-200 hPa, 250-300 hPa). This is of interest since future commercial aircraft could be

optimised to fly at other altitudes to mitigate the projected increase in MOG-CAT frequency found at the current cruising altitudes. Furthermore, in-flight turbulence data could be used to study the reliability of CAT indices. In particular over the North Atlantic, this would provide a better understanding of CAT generation mechanisms and reduce MOG-CAT projection uncertainties. Collaborations with government agencies regulators of civil aviation and airlines are necessary to have access to these in-flight measurements.

Future research is also needed to investigate future changes in CAT intensity together with wind gust to define the maximum load an aircraft can withstand. To study properly the impact of CAT extreme intensities on a commercial aircraft, spatial scales ranging from 100 m to 2 km are suitable. The use of dynamical downscaling approaches, in which a regional model is nested by a coarser resolution global model, could be of interest to address future changes in CAT intensity over a certain region.

Open Research

The ERA5 reanalysis on pressure levels can be downloaded here: https://cds.climate.copernicus.eu/cdsapp#!/dataset/reanalysis-era5-pressure-levels?tab=form, JRA55 were obtained from: https://rda.ucar.edu/datasets/ds628.0/index.html#!access, and MERRA-2 can be downloaded from: https://disc.gsfc.nasa.gov/datasets?project=MERRA-2. All CMIP6 data analyzed in this study were obtained from the Institut Pierre Simon Laplace (IPSL) node of the Earth System Grid Federation (ESGF): https://esgf-node.ipsl.upmc.fr/search/cmip6-ipsl/. The 20 simulations performed with CNRM-CM6-1 model can be provided by the authors upon request.

Acknowledgments

The authors thanks the climate modeling groups for producing the CMIP6 data and the Earth System Grid Federation (ESGF) for archiving the data and providing access freely available. We gratefully thank Marie-Pierre Moine and Laure Coquart for their help to handle the CNRM-CM6-1 climate model. The authors thank the CNRM-CERFACS modeling group for developing and supporting the CNRM-CM6-1 model. We thank P. D. Williams for valuable comments on this work, for the helpful discussions and for hosting M. Foudad at the University of Reading in June 2023, we would also aknowledge Didier Ricard from Météo-France/CNRM and Marc Wetterwald from Airbus for helpful discussions.

References

Boucher, O., Servonnat, J., Albright, A. L., Aumont, O., Balkanski, Y., Bastrikov, V., ... others (2020). Presentation and evaluation of the IPSL-CM6A-LR climate model. *Journal of Advances in Modeling Earth Systems*, *12*(7), e2019MS002010. doi: https://doi.org/10.1029/2019MS002010

Deser, C., Phillips, A. S., Alexander, M. A., & V, S. B. (2014). Projecting North American climate over the next 50 years: uncertainty due to internal variability. *Journal of Climate*, *27*(6), 2271–2296. doi: https://doi.org/10.1175/JCLI-D-13-00451.1

Deser, C., Phillips, A. S., Bourdette, V., & Teng, H. (2012). Uncertainty in climate change projections: the role of internal variability. *Climate Dynamics*, *38*, 527–546. doi: https://doi.org/10.1007/s00382-010-0977-x

Deser, C., Terray, L., & Phillips, A. S. (2016). Forced and internal components of winter air temperature trends over north america during the past 50 years: Mechanisms and implications. *Journal of Climate*, *29*(6), 2237–2258. doi:

http://dx.doi.org/10.1175/JCLI-D-15-0304.s1

Döscher, R., Acosta, M., Alessandri, A., Anthoni, P., Arneth, A., Arsouze, T., ... others (2021). The EC-Earth3 Earth system model for the Coupled Model Intercomparison Project 6. *Geoscientific Model Development Discussions*, *2021*, 1–90. doi: https://doi.org/10.5194/gmd-15-2973-2022

Dutton, J. A., & Panofsky, H. A. (1970). Clear air turbulence: A mystery may be unfolding: High altitude turbulence poses serious problems for aviation and atmospheric science. *Science*, *167*(3920), 937–944. doi: https://doi.org/10.1126/science.167.3920.937

Ellrod, G. P., & Knapp, D. I. (1992). An objective clear-air turbulence forecasting technique: Verification and operational use. *Weather and Forecasting*, *7*(1), 150–165. doi: https://doi.org/10.1175/1520-0434(1992)007%3C0150:AOCATF%3E2.0.CO;2

Ellrod, G. P., Knox, J. A., Lester, P. F., & Ehernberger, L. J. (2015). Clear air turbulence. In G. R. North, J. Pyle, & F. Zhang (Eds.), *Encyclopedia of atmospheric science, 2nd edn* (pp. 177–186). Elsevier. doi: https://doi.org/10.1016/B978-0-12-382225-3.00104-3

Eyring, V., Bony, S., Meehl, G. A., A, S. C., Stevens, B., Stouffer, R. J., & Taylor, K. E. (2016). Overview of the Coupled Model Intercomparison Project Phase 6 (CMIP6) experimental design and organization. *Geoscientific Model Development*, *9*(5), 1937–1958. doi: https://doi.org/10.5194/gmd-9-1937-2016

Gelaro, R., McCarty, W., Suárez, M. J., Todling, R., Molod, A., Takacs, L., ... Zhao, B. (2017). The Modern-Era Retrospective Analysis for Research and Applications, Version 2 (MERRA-2). *Journal of Climate*, *30*(14), 5419–5454. doi: https://doi.org/10.1175/JCLI-D-16-0758.1

Gill, P. G. (2014). Objective verification of World Area Forecast Centre clear air turbulence forecasts. *Meteorological Applications*, *21*(1), 3–11. doi: https://doi.org/10.1002/met.1288

Gultepe, I., Sharman, R., Williams, P., Zhou, B., Ellrod, G., Minnis, P., ... Neto, F. (2019). A review of high impact weather for aviation meteorology. *Pure and Applied Geophysics*, *176*, 1869–1921. doi: https://doi.org/10.1007/s00024-019-02168-6

Hajima, T., Watanabe, M., Yamamoto, A., Tatebe, H., Noguchi, M. A., Abe, M., ... others (2020). Development of the MIROC-ES2L Earth system model and the evaluation of biogeochemical processes and feedbacks. *Geoscientific Model Development*, *13*(5), 2197–2244. doi: https://doi.org/10.5194/gmd-13-2197-2020

Hawkins, E., & Sutton, R. (2011). The potential to narrow uncertainty in projections of regional precipitation change. *Climate dynamics*, *37*, 407–418. doi: https://doi.org/10.1007/s00382-010-0810-6

Hersbach, H., Bell, B., P., B., Hirahara, S., Horányi, A., Muñoz-Sabater, J., ... Thépaut, J. (2020). The ERA5 global reanalysis. *Quarterly Journal of the Royal Meteorological Society*, *146*(730), 1999–2049. doi: https://doi.org/10.1002/qj.3803

Jaeger, E. B., & Sprenger, M. (2007). A Northern Hemispheric climatology of indices for clear air turbulence in the tropopause region derived from ERA40 reanalysis data. *Journal of Geophysical Research: Atmospheres*, *112*(D20). doi: https://doi.org/10.1029/2006JD008189

Kay, J. E., Deser, C., Phillips, A., Mai, A., Hannay, C., Strand, G., ... Vertenstein, M. (2015). The Community Earth System Model (CESM) large ensemble project: A community resource for studying climate change in the presence of internal climate variability. *Bulletin of the American Meteorological Society*, *96*(8), 1333–1349. doi: https://doi.org/10.1175/BAMS-D-13-00255.1

Kim, J.-H., Sharman, R., Strahan, M., Scheck, J. W., Bartholomew, C., Cheung, J. C., ... Gait, N. (2018). Improvements in nonconvective aviation turbulence prediction for the world area forecast system. *Bulletin of the American Meteorological Society*, *99*(11), 2295–2311. doi: https://doi.org/10.1175/BAMS-D-17-0117.1

Kobayashi, S., Ota, Y., Harada, Y., Ebita, A., Moriya, M., Onoda, H., ... others (2015).

The JRA-55 reanalysis: General specifications and basic characteristics. *Journal of the Meteorological Society of Japan. Ser. II*, *93*(1), 5–48. doi: https://doi.org/10.2151/jmsj.2015-001

Lee, J. H., Kim, J.-H., Sharman, R. D., Kim, J., & Son, S.-W. (2023). Climatology of clear-air turbulence in upper troposphere and lower stratosphere in the Northern Hemisphere using ERA5 reanalysis data. *Journal of Geophysical Research: Atmospheres*, *128*(1), e2022JD037679. doi: https://doi.org/10.1029/2022jd037679

Lee, S. H., Williams, P. D., & Frame, T. H. (2019). Increased shear in the North Atlantic upper-level jet stream over the past four decades. *Nature*, *572*(7771), 639–642. doi: https://doi.org/10.1038/s41586-019-1465-z

Lv, Y., Guo, J., Li, J., Han, Y., Xu, H., Guo, X., ... Gao, W. (2021). Increased Turbulence in the Eurasian upper-level jet stream in winter: Past and future. *Earth and Space Science*, *8*(2), e2020EA001556. doi: https://doi.org/10.1029/2020EA001556

Masson-Delmotte, V., Zhai, P., Pirani, A., Connors, S. L., Péan, C., Berger, S., ... Zhou, B. (2021). *IPCC: Climate Change 2021 – The Physical Science Basis: Working Group I Contribution to the Sixth Assessment Report of the Intergovernmental Panel on Climate Change*. Cambridge, United Kingdom and New York, NY, USA: Cambridge University Press. doi: https://doi.org/10.1017/9781009157896

Müller, W. A., Jungclaus, J. H., Mauritsen, T., Baehr, J., Bittner, M., Budich, R., ... others (2018). A high-resolution version of the Max Planck Institute Earth System Model (MPI-ESM1. 2-HR). *Journal of Advances in Modeling Earth Systems*, *10*(7), 1383–1413. doi: https://doi.org/10.1029/2017MS001217

O'Neill, B. C., Tebaldi, C., Van Vuuren, D. P., Eyring, V., Friedlingstein, P., Hurtt, G., ... others (2016). The Scenario Model Intercomparison Project (ScenarioMIP) for CMIP6. *Geoscientific Model Development*, *9*(9), 3461–3482. doi: https://doi.org/10.5194/gmd-9-3461-2016

Overeem, A. (2002). *Verification of clear-air turbulence forecasts* (Tech. Rep.). KNMI (Royal Netherlands Meteorological Institute).

Seland, Ø., Bentsen, M., Olivié, D., Toniazzo, T., Gjermundsen, A., Graff, L. S., ... others (2020). Overview of the Norwegian Earth System Model (NorESM2) and key climate response of CMIP6 DECK, historical, and scenario simulations. *Geoscientific Model Development*, *13*(12), 6165–6200. doi: https://doi.org/10.5194/gmd-13-6165-2020

Sellar, A. A., Jones, C. G., Mulcahy, J. P., Tang, Y., Yool, A., Wiltshire, A., ... others (2019). UKESM1: Description and evaluation of the UK Earth System Model. *Journal of Advances in Modeling Earth Systems*, *11*(12), 4513–4558. doi: https://doi.org/10.1029/2019MS001739

Sharman, R., & Lane, T. (2016). *Aviation turbulence: Processes, detection, and prediction*. Berlin: Springer. doi: https://doi.org/10.1007/978-3-319-23630-8

Sharman, R., Tebaldi, C., Wiener, G., & Wolff, J. (2006). An integrated approach to mid-and upper-level turbulence forecasting. *Weather and forecasting*, *21*(3), 268–287. doi: https://doi.org/10.1175/WAF924.1

Sharman, R., Trier, S., Lane, T., & Doyle, J. (2012). Sources and dynamics of turbulence in the upper troposphere and lower stratosphere: A review. *Geophysical Research Letters*, *39*(12). doi: https://doi.org/10.1029/2012GL051996

Shaw, T., Baldwin, M., Barnes, E. A., Caballero, R., Garfinkel, C., Hwang, Y.-T., ... others (2016). Storm track processes and the opposing influences of climate change. *Nature Geoscience*, *9*(9), 656–664. doi: https://doi.org/10.1038/ngeo2783

Smith, I. H., Williams, P. D., & Schiemann, R. (2023). Clear-air turbulence trends over the North Atlantic in high-resolution climate models. *Climate Dynamics*, 1–17. doi: https://doi.org/10.1007/s00382-023-06694-x

Storer, L. N., Gill, P. G., & Williams, P. D. (2020). Multi-diagnostic multi-model ensemble forecasts of aviation turbulence. *Meteorological Applications*, *27*(1), e1885. doi: https://doi.org/10.1002/met.1885

Storer, L. N., Williams, P. D., & Gill, P. G. (2019). Aviation turbulence: dynamics, forecasting, and response to climate change. *Pure and Applied Geophysics*, *176*, 2081–2095. doi: https://doi.org/10.1007/s00024-018-1822-0

Storer, L. N., Williams, P. D., & Joshi, M. M. (2017). Global response of clear-air turbulence to climate change. *Geophysical Research Letters*, *44*(19), 9976–9984. doi: https://doi.org/10.1002/2017GL074618

Swart, N. C., Cole, J. N., Kharin, V. V., Lazare, M., Scinocca, J. F., Gillett, N. P., ... others (2019). The Canadian Earth System Model version 5 (CanESM5. 0.3). *Geoscientific Model Development*, *12*(11), 4823–4873. doi: https://doi.org/10.5194/gmd-12-4823-2019

Tatebe, H., Ogura, T., Nitta, T., Komuro, Y., Ogochi, K., Takemura, T., ... others (2019). Description and basic evaluation of simulated mean state, internal variability, and climate sensitivity in MIROC6. *Geoscientific Model Development*, *12*(7), 2727–2765. doi: https://doi.org/10.5194/gmd-12-2727-2019

Tenenbaum, J., Williams, P. D., Turp, D., Buchanan, P., Coulson, R., Gill, P. G., ... Rukhovets, L. (2022). Aircraft observations and reanalysis depictions of trends in the North Atlantic winter jet stream wind speeds and turbulence. *Quarterly Journal of the Royal Meteorological Society*, *148*(747), 2927–2941. doi: https://doi.org/10.1002/qj.4342

Uppala, S. M., Kållberg, P., Simmons, A. J., Andrae, U., Bechtold, V. D. C., Fiorino, M., ... others (2005). The ERA-40 re-analysis. *Quarterly Journal of the Royal Meteorological Society: A journal of the atmospheric sciences, applied meteorology and physical oceanography*, *131*(612), 2961–3012. doi: https://doi.org/10.1256/qj.04.176

Voldoire, A., Saint-Martin, D., Sénési, S., Decharme, B., Alias, A., Chevallier, M., ... others (2019). Evaluation of CMIP6 deck experiments with CNRM-CM6-1. *Journal of Advances in Modeling Earth Systems*, *11*(7), 2177–2213. doi: https://doi.org/10.1029/2019MS001683

Volodin, E., Mortikov, E., Kostrykin, S., Galin, V. Y., Lykossov, V., Gritsun, A., ... Iakovlev, N. (2017). Simulation of the present-day climate with the climate model INMCM5. *Climate dynamics*, *49*, 3715–3734. doi: https://doi.org/10.1007/s00382-017-3539-7

Williams, K., Copsey, D., Blockley, E., Bodas-Salcedo, A., Calvert, D., Comer, R., ... others (2018). The Met Office global coupled model 3.0 and 3.1 (GC3. 0 and GC3. 1) configurations. *Journal of Advances in Modeling Earth Systems*, *10*(2), 357–380. doi: https://doi.org/10.1002/2017MS001115

Williams, P. D. (2016). Transatlantic flight times and climate change. *Environmental Research Letters*, *11*(2), 024008. doi: http://dx.doi.org/10.1088/1748-9326/11/2/024008

Williams, P. D. (2017). Increased light, moderate, and severe clear-air turbulence in response to climate change. *Advances in Atmospheric Sciences*, *34*(5), 576–586. doi: https://doi.org/10.1007/s00376-017-6268-2

Williams, P. D., & Joshi, M. M. (2013). Intensification of winter transatlantic aviation turbulence in response to climate change. *Nature Climate Change*, *3*(7), 644–648. doi: https://doi.org/10.1038/nclimate1866

Williams, P. D., & Storer, L. N. (2022). Can a climate model successfully diagnose clear-air turbulence and its response to climate change? *Quarterly Journal of the Royal Meteorological Society*, *148*(744), 1424–1438. doi: https://doi.org/10.1002/qj.4270

Table 1. *List of CMIP6 Climate Models Used in this Study with the Experiments Used and Number of Members. The Spatial Resolution and the Reference Paper of Each Model are also Provided*

Model	Historical members	SSP5-8.5 members	Spatial resolution	reference
$CNRM-CM6-1$	20	20	$1.4° \times 1.4°$	Voldoire et al. (2019)
$IPSL-CM6A-LR$	33	7	$2.5° \times 1.3°$	Boucher et al. (2020)
$CanESM5$	10	10	$2.8° \times 2.8°$	Swart et al. (2019)
$MIROC-ES2L$	10	10	$2.8° \times 2.8°$	Hajima et al. (2020)
$UKESM1-0-LL$	5	5	$1.875° \times 1.25°$	Sellar et al. (2019)
$HadGEM3-GC31-LL$	4	4	$1.875° \times 1.25°$	K. Williams et al. (2018)
$EC-Earth3$	3	3	$0.7° \times 0.7°$	Döscher et al. (2021)
$MIROC6$	3	3	$1.4° \times 1.4°$	Tatebe et al. (2019)
$INM-CM5$	1	1	$2° \times 1.5°$	Volodin et al. (2017)
$MPI-ESM1-2-HR$	1	1	$0.9° \times 0.9°$	Müller et al. (2018)
$NorESM2-LM$	1	1	$2.5° \times 1.9°$	Seland et al. (2020)

Note. CMIP6, Coupled Model Intercomparison Project Phase 6; SSP5-8.5; Shared Socio-economic Pathway 5.

Table 2. *Percentage of Change in winter MOG-CAT Frequency for the Period 1980-2021 over the Four Regions Indicated in the Boxes in (Figure 5). The Methodology to Compute the Percentage of Change is Detailed in the Text. Bold Police Indicate Those Changes that are Significant at the 99% Level (p value < 0.01) by Using a two-tailed t test.*

Reanalysis	Northern NA			Southern NA		
	TI1	VWS	DEF	TI1	VWS	DEF
ERA5	55.4	38.4	33.3	**112.7**	**120.7**	75.2
JRA55	65.8	47.7	43.6	**197.9**	**308.7**	91.4
MERRA2	64.2	69.5	31.8	**157.3**	**151.1**	74.3

Reanalysis	North Pacific			Middle-East/East-Asia		
	TI1	VWS	DEF	TI1	VWS	DEF
ERA5	**63.1**	45.9	-8.8	**82.6**	**116.6**	59.3
JRA55	**63.2**	56.0	-1.8	**164.4**	**330.8**	**109.6**
MERRA2	**56.9**	**70.9**	-11.6	**71.0**	**84.9**	51.2

Note. MOG-CAT, Moderate-Or-Greater Clear-Air Turbulence; NA, North Atlantic; TI1, Turbulence Index 1; VWS, vertical wind shear; DEF, flow deformation.

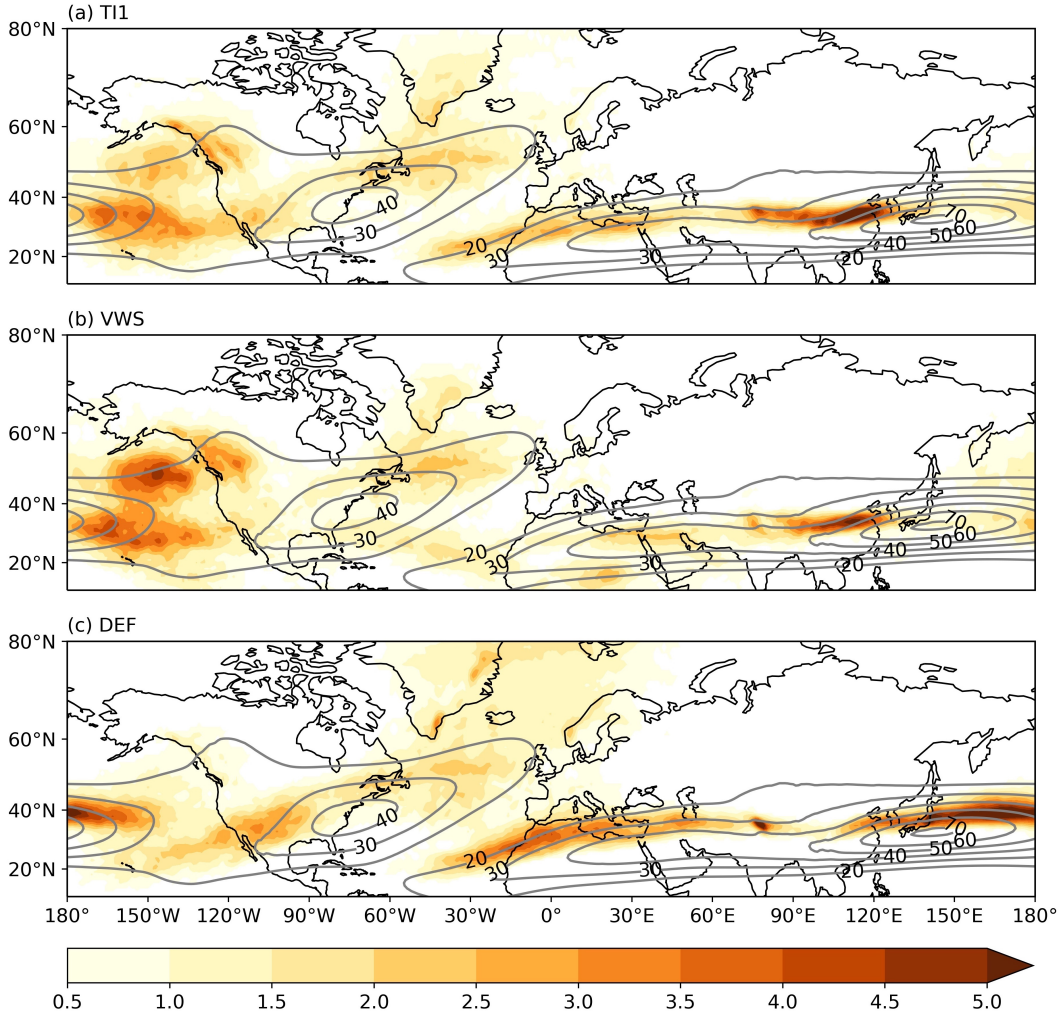

Figure 1. Winter (DJF) climatology of MOG-CAT frequency (≥ 0.5) for (a) Turbulence Index 1 (TI1), (b) Vertical Wind Shear (VWS), (c) Flow Deformation (DEF) at 200-250 hPa from 1981 to 2010 based on ERA5 reanalysis. Zonal wind speed climatology at 250 hPa level is shown by the black contours (every 10 m s^{-1}, for wind speeds $\geq$ 20 m s^{-1}). Units are in %.

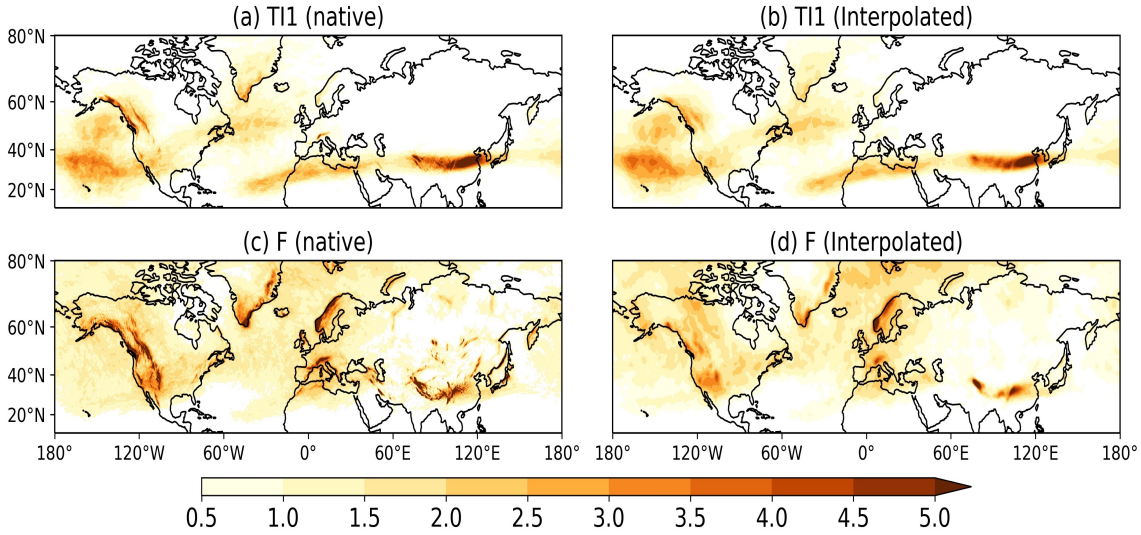

Figure 2. Winter (DJF) climatology of MOG-CAT frequency (≥ 0.5) at 200-250 hPa from 1981 to 2010 based on ERA5 native grid (left) and interpolated grid (right) for (a-b) Turbulence index 1 (TI1), (c-d) frontogenesis function. Units are in %.

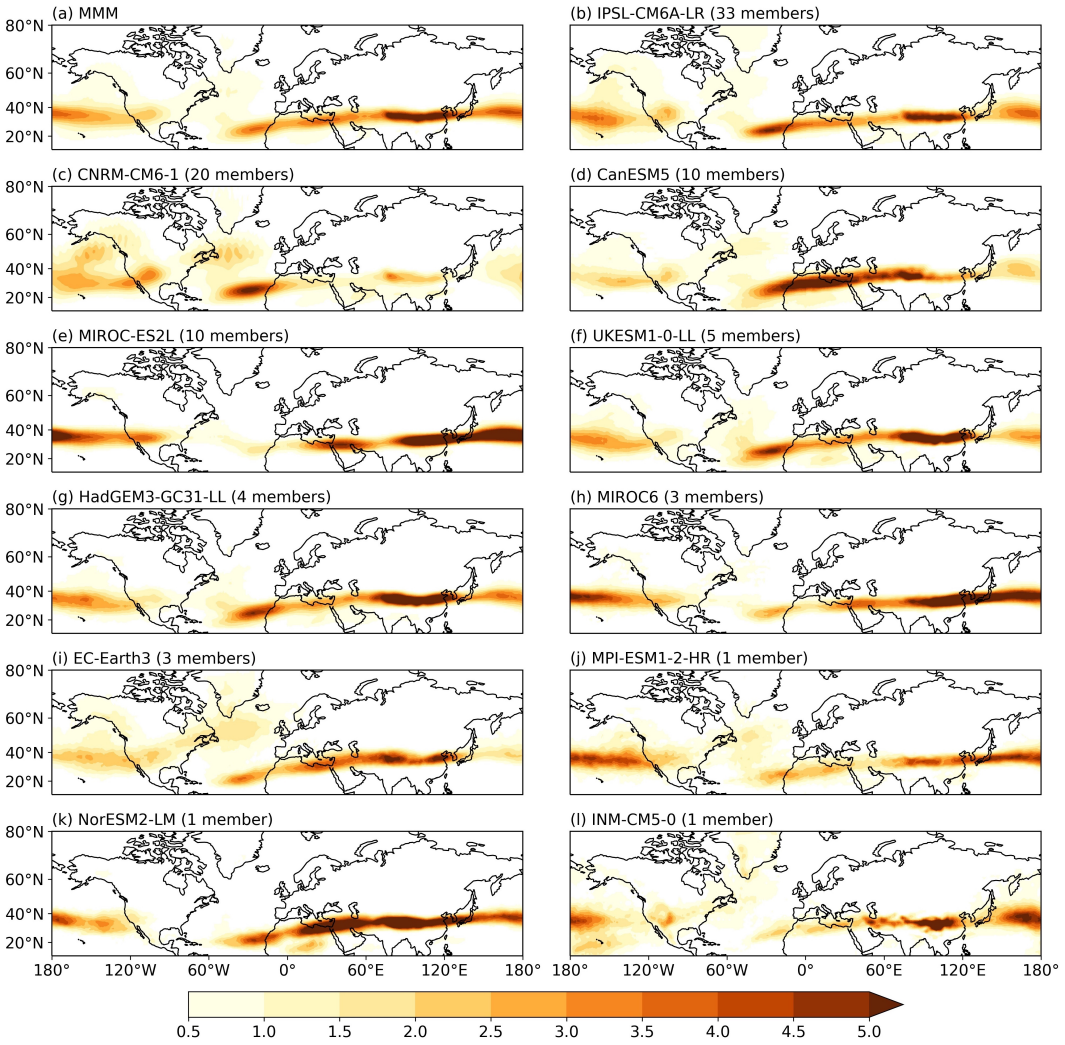

Figure 3. Winter (DJF) climatology of MOG-CAT frequency (≥ 0.5) of the Turbulence Index 1 at 200-250 hPa between 1981-2010 from (a) Multi-Model ensemble Mean (MMM) and (b-l) different CMIP6 climate models. Units are in %.

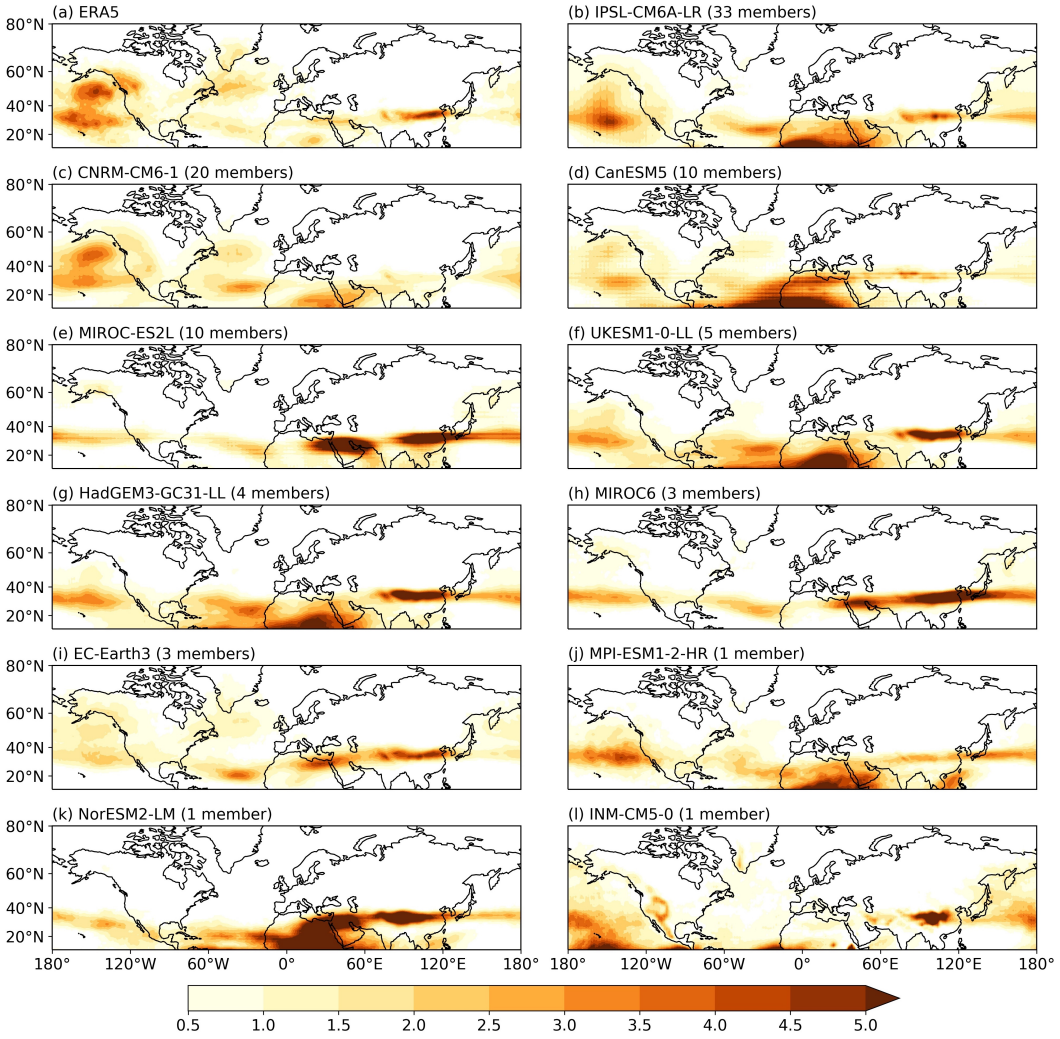

Figure 4. Winter (DJF) climatology of MOG-CAT frequency ($\geq 0.5\%$) of vertical wind shear diagnostic at 200-250 hPa between 1981-2010 from (a) ERA5 reanalysis and (b-l) different CMIP6 climate models. Units are in %.

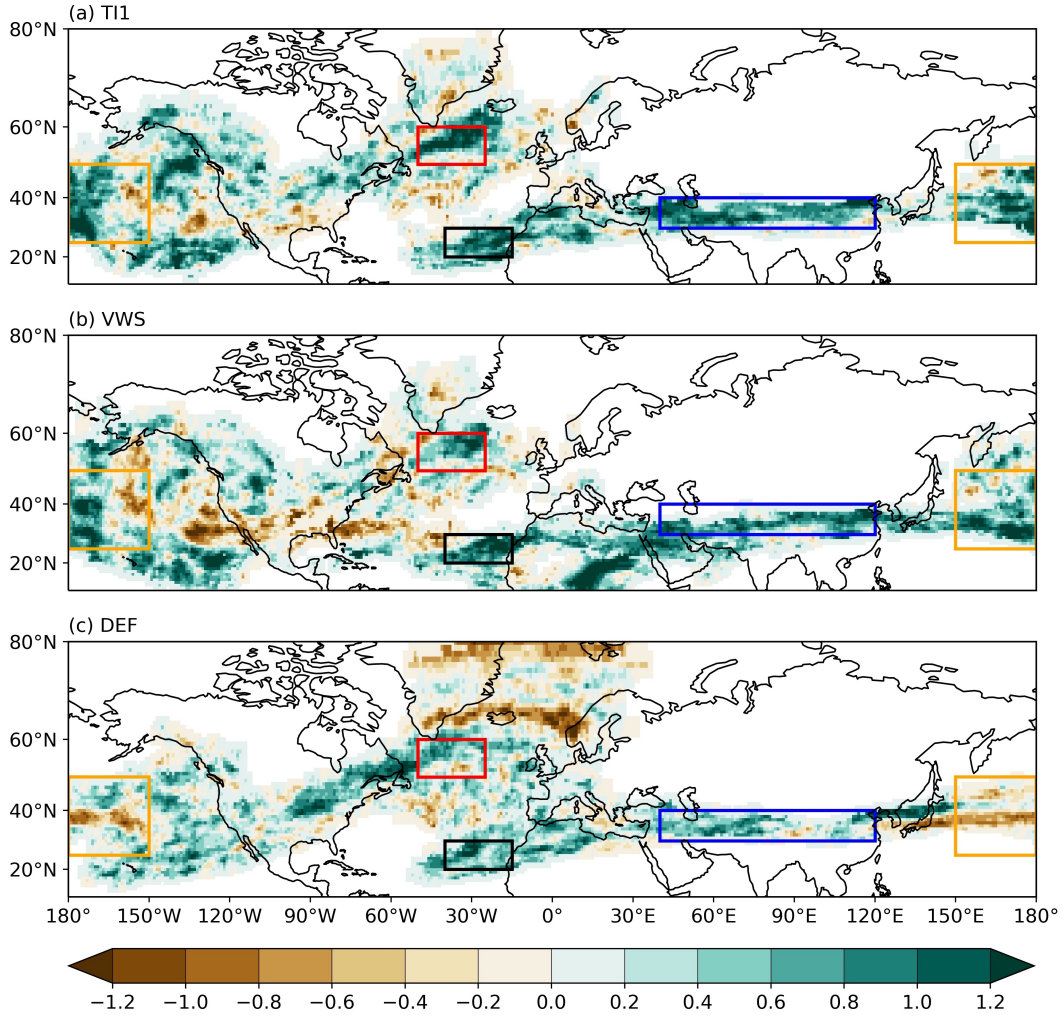

Figure 5. Ratio between the value of the trend and the interannual variability for MOG-CAT frequency estimated over the period 1980-2021 from ERA5 for (a) Turbulence Index 1 (TI1), (b) Vertical Wind Shear (VWS), (c) Flow Deformation (DEF) at 200-250 hPa for the winter season. Red, black, blue and orange boxes indicate Northern North Atlantic (NA) (50-25°W, 50-60°N), Southern NA (40-15°W, 20-30°N), Middle-East and East-Asia (40-120°E, 30-40°N), North Pacific (150°E-150°W, 25-50°N) regions respectively.

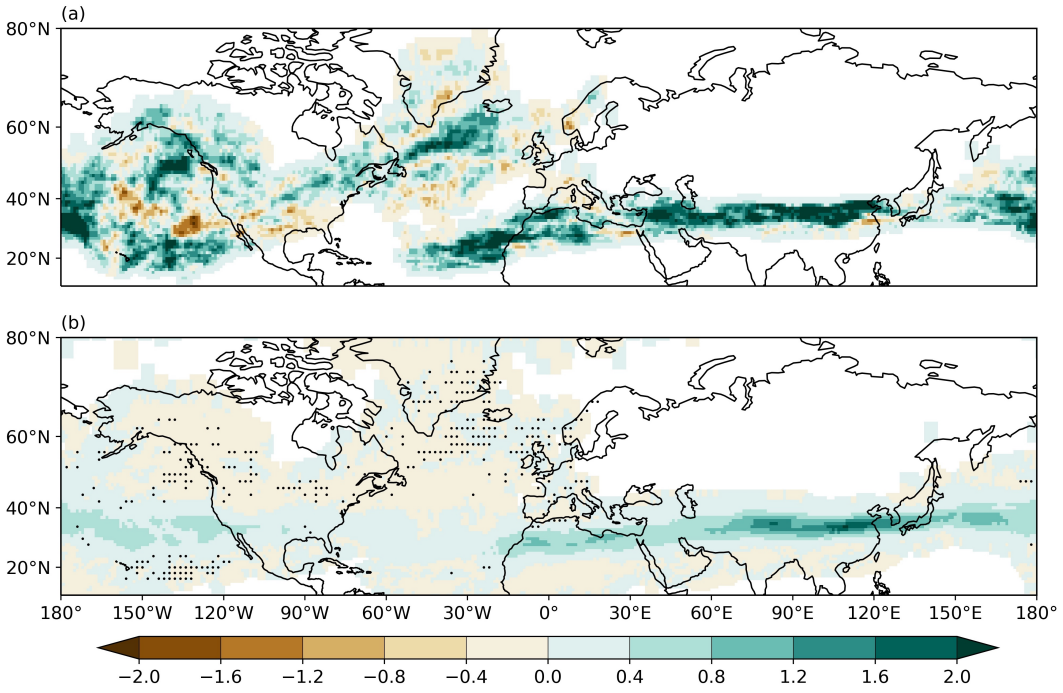

Figure 6. Winter (DJF) MOG-CAT frequency trends for Turbulence index 1 at 200-250 hPa over the period 1980-2021 from (a) ERA5 reanalysis, (b) The multi-model ensemble mean. The black dots in (b) indicate where the observed MOG-CAT trend in ERA5 is outside the range of the forced trends in the multi-model ensemble members.

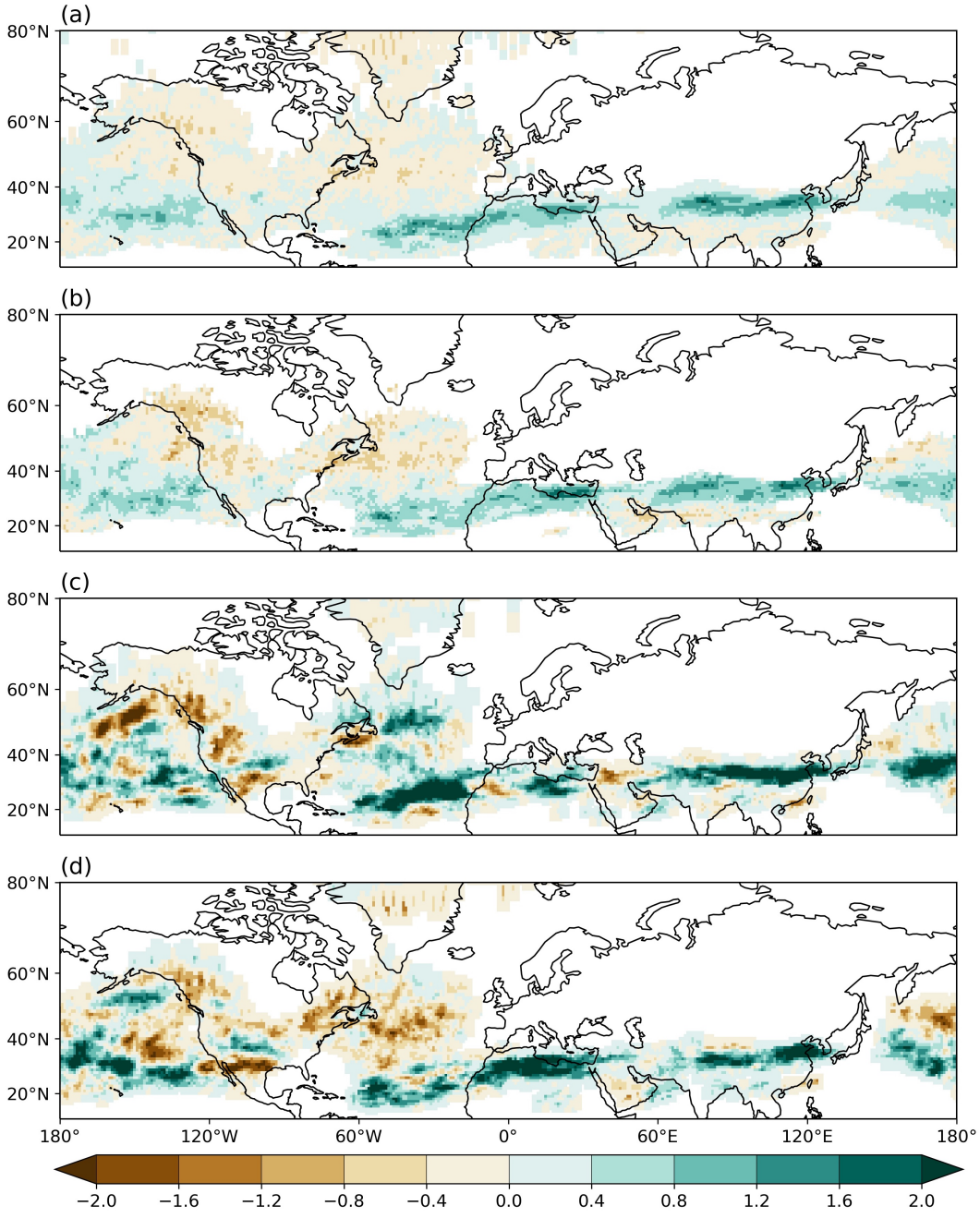

Figure 7. Winter (DJF) MOG-CAT frequency trends for Turbulence index 1 at 200-250 hPa over the period 1980-2021 from (a) The CNRM-CM6-1 model ensemble mean, (c) member 15, (d) member 16. (b) Signal-to-noise ratio from the 20 CNRM-CM6-1 ensemble members.

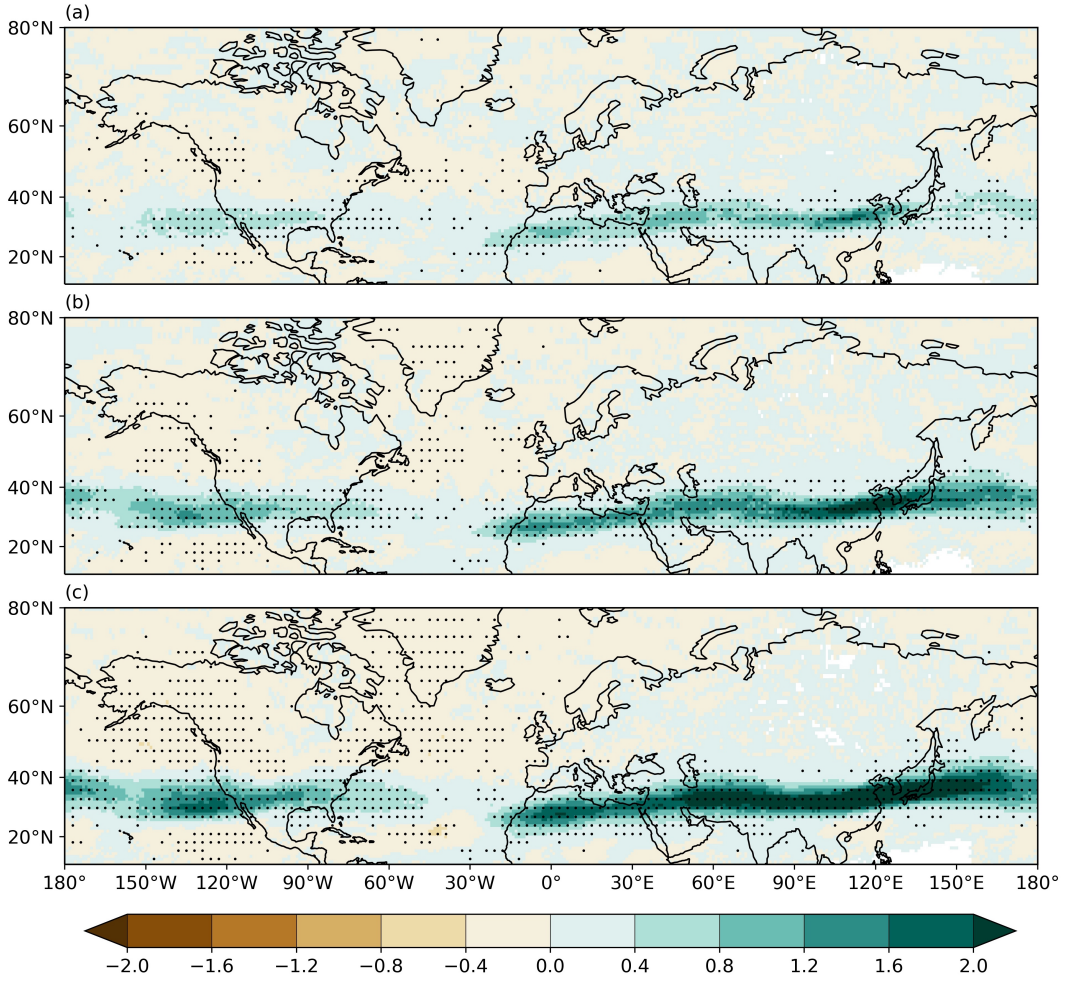

Figure 8. Projected changes in MOG-CAT frequency for Turbulence Index 1 at different global warming levels explained in the text: (a) ΔT=1°C, (b) ΔT=2°C and (c) ΔT=3°C. Changes are estimated from the multi-model ensemble mean. The black dots indicate those grid points where more than 80% of models agree on the sign of the change. Units are in %.

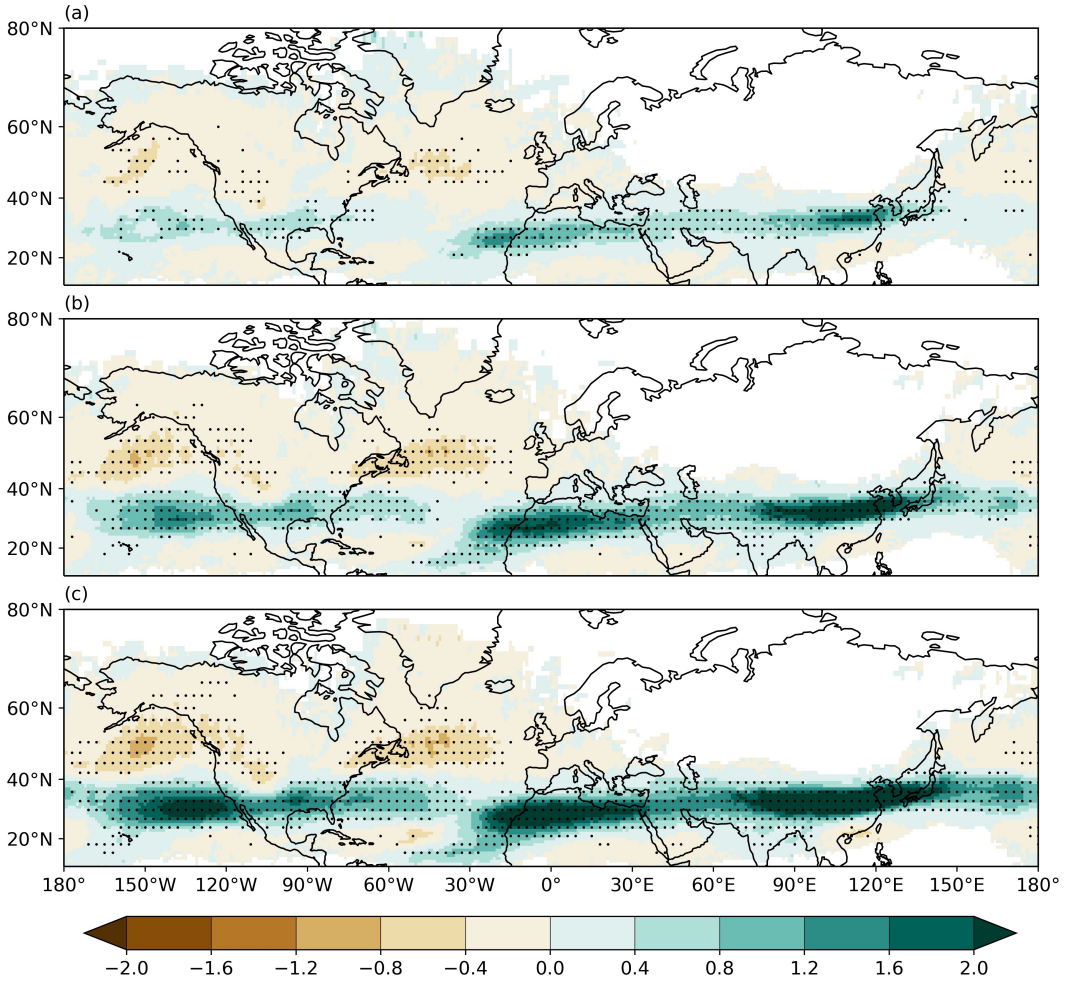

Figure 9. Projected changes in MOG-CAT frequency for Turbulence Index 1 at different global warming levels explained in the text: (a) ΔT=1°C, (b) ΔT=2°C and (c) ΔT=3°C. Changes are estimated from the CNRM-CM6-1 model ensemble mean. The black dots indicate those grid points where more than 80% of members agree on the sign of the change. Units are in %.

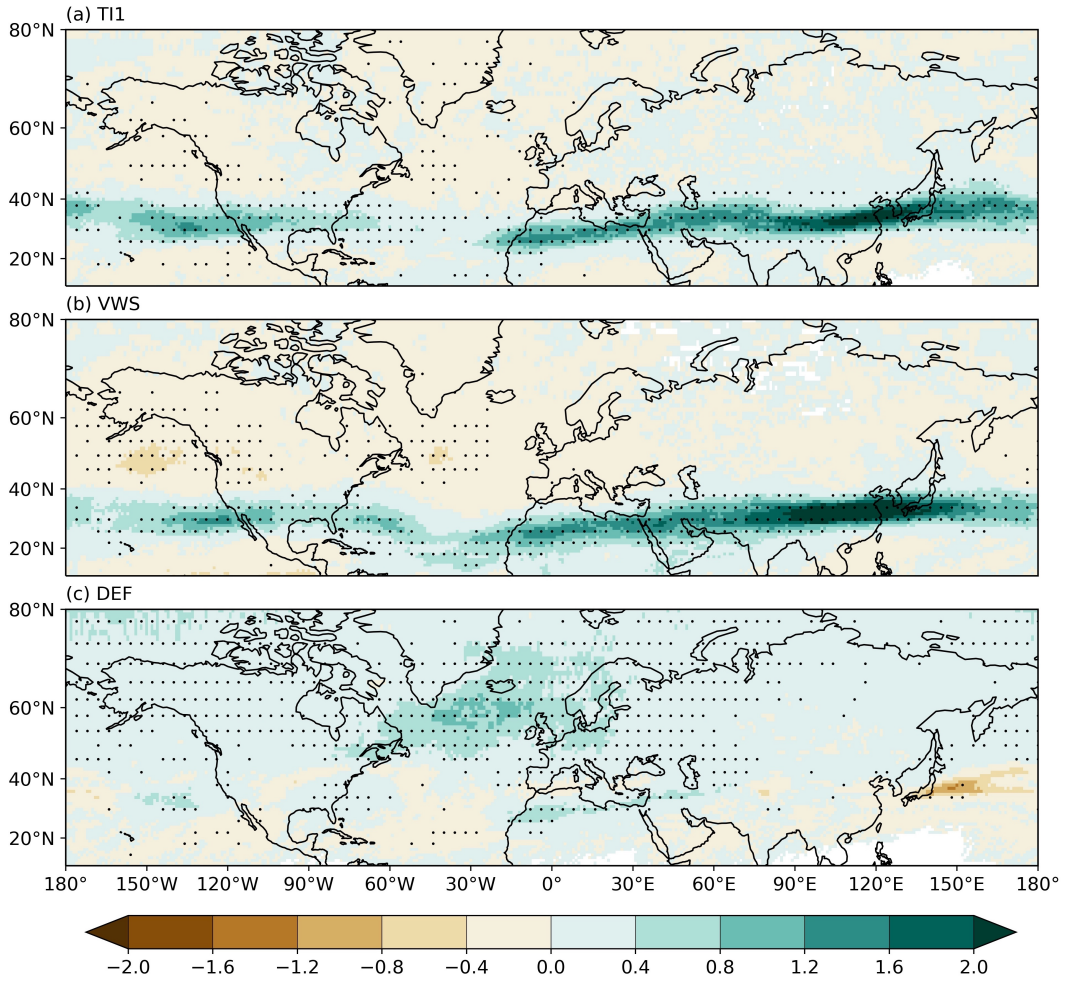

Figure 10. Projected changes in MOG-CAT frequency at ΔT=2°C for (a) Turbulence Index 1 (TI1), (b) Vertical Wind Shear (VWS), (c) Flow Deformation (DEF). Changes are estimated from the multi-model ensemble mean. The black dots indicate those grid points where more than 80% of models agree on the sign of the change. Units are in %.

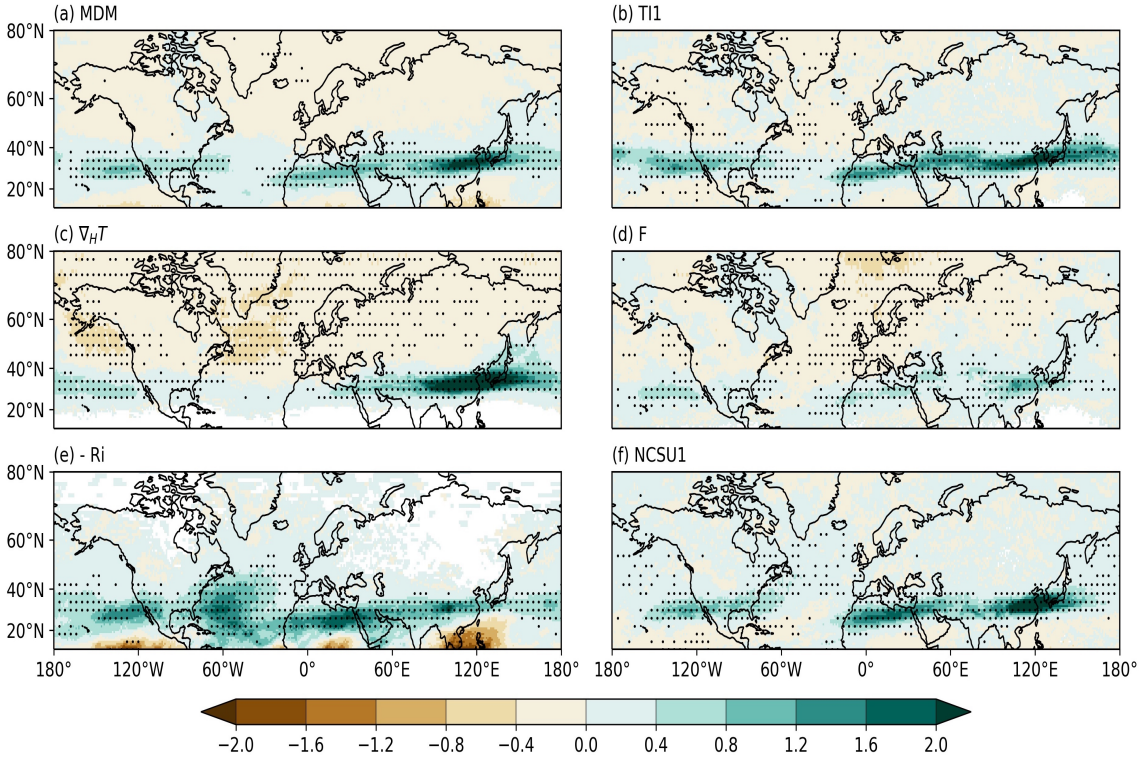

Figure 11. Projected changes in MOG-CAT frequency at ΔT=2°C for (a) the multi-diagnostic mean (MDM), (b) Turbulence Index 1 (TI1), (c) horizontal temperature gradient ($\nabla_H T$), (d) Frontogenesis function (F), (e) negative Richardson number (- Ri), and (f) North Carolina State University index 1 (NCSU1). Changes are estimated from the multi-model ensemble mean. The black dots in (a) indicate those grid points where all CAT indices agree on the sign of the change, while in (b-f) they indicates where more than 80% of models agree on the sign of the change. Units are in %.